J. Fluid Mech. (2022), *vol*. 932, A50, doi:10.1017/jfm.2021.1033

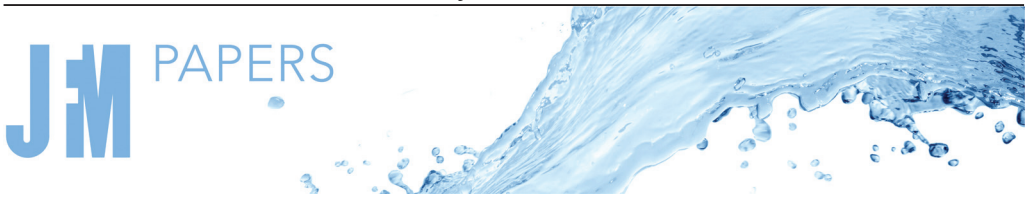

Bolus formation from fission of nonlinear internal waves over a mild slope

Amin Ghassemi[1],†, **Saeid Zahedi**[1] **and Leon Boegman**[1]

[1]Environmental Fluid Dynamics Laboratory, Department of Civil Engineering, Queen's University, 58 University Avenue, Kingston, Ontario K7L 3N6, Canada

(Received 14 February 2021; revised 26 October 2021; accepted 17 November 2021)

Breaking nonlinear internal waves (NLIWs) of depression on boundary slopes drives mixing in the coastal ocean. Of the different breaker types, fission is most commonly observed on mild slopes of continental margins. However, fission on mild slopes has rarely been investigated in the laboratory owing to limitations on flume length. In the present work, a train of NLIWs of depression is generated in an 18.2 m wave flume and shoaled upon a mild uniform slope. During fission, each NLIW of depression scatters into one or two NLIWs of elevation, which transforms into a bolus at the bolus birth point, where shear instability occurs through the pycnocline. The bolus propagates upslope, decreasing in size until it degenerates by shear and lobe-cleft instability, while losing volume to a return flow along the bed. The location of the bolus birth point, bolus propagation length scale, initial size and the number of boluses from each incident wave are parameterized from the wave half-width and the wave Froude number associated with the incident NLIW. These are compared with the characteristics of boluses generated by other breaking mechanisms on steeper slopes. Some bolus characteristics (height to length ratio, change in size and velocity field) are similar for boluses generated by fission, collapsing sinusoidal waves and internal solitary waves of elevation; however, the number of boluses, their birth point and initial height differ. The boluses formed by fission have more initial energy and no reflection. Further research is required to better quantify bolus-driven mixing on continental margins.

Key words: coastal engineering, internal waves, stratified flows

1. Introduction

Nonlinear internal waves (NLIWs) are ubiquitous phenomena of stratified lakes and coastal oceans (Jackson 2007, their figure 1; Osborne & Burch 1980; Boegman & Ivey 2009; Boegman & Stastna 2019) where they can freely travel for hundreds of

† Email address for correspondence: amin.ghassemi@queensu.ca

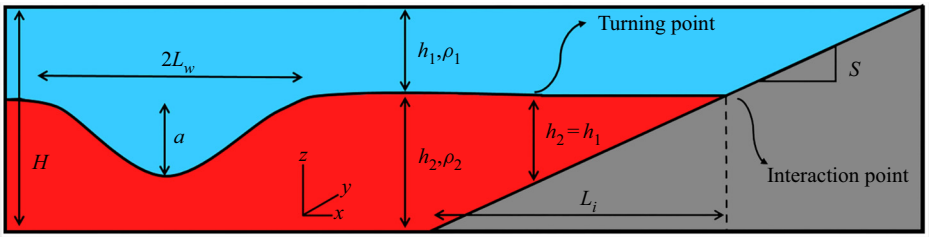

Figure 1. Schematic showing the propagation of an NLIW of depression in a two-layer stratification system toward a uniform boundary slope. Here the total depth (H) consists of a thicker (h_2) and commonly denser (ρ_2) lower layer which is overlaid by a thinner (h_1) and lower denser (ρ_1) layer. An NLIW of depression with amplitude a and wavelength $\lambda = 2L_w$ propagates towards a planer slope with steepness S. Here, L_i is the pycnocline length above the slope.

kilometres before losing their energy through turbulent mixing and viscous dissipation during shoaling and breaking (Apel 2002; Boegman, Ivey & Imberger 2005; Shroyer, Moum & Nash 2009; Barad & Fringer 2010). The formation of NLIWs in oceans, through tide–topography interactions (Apel *et al.* 1985; Lamb 1994), is different from that in lakes, where they form by nonlinear steepening of basin-scale internal seiches (Horn, Imberger & Ivey 2001; Boegman & Ivey 2009). Shoaling and breaking of NLIWs on sloping boundaries lead to localized mixing of the background density stratification (Wunsch 1971; Wüest, Piepke & Van Senden 2000; Allshouse & Swinney 2020), drive vertical biogeochemical fluxes (Haury, Briscoe & Orr 1979; Sandstrom & Elliott 1984; Scotti & Pineda 2007) and energize sediment resuspension and transport along continental margins (Southard & Cacchione 1972; Pomar *et al.* 2012; Ma *et al.* 2016).

Experimental and numerical studies on NLIW shoaling and breaking on slopes can be categorized into three groups: (1) breaking over idealized continental slope-shelf topography (Helfrich & Melville 1986; Venayagamoorthy & Fringer 2007; Lim, Ivey & Jones 2010; Lamb & Xiao 2014); (2) breaking over a uniform slope (Wallace & Wilkinson 1988; Boegman & Ivey 2009; Aghsaee, Boegman & Lamb 2010; Nakayama *et al.* 2019; Xu & Stastna 2020); and (3) breaking over realistic topography (Vlasenko & Stashchuk 2007; Lamb & Warn-Varnas 2015; Masunaga *et al.* 2017; Rivera-Rosario *et al.* 2020; Guo, Zhan & Hoteit 2021). Uniform slope topography (figure 1) is common to the margins of lakes, fjords and some coastal regions, e.g. Mono Lake (MacIntyre *et al.* 1999), Lake Biwa (Boegman *et al.* 2003), Lake Michigan (Hawley 2004), the Oregon continental shelf (Klymak & Moum 2003), the Alboran slope (Puig *et al.* 2004), the Australian North West Shelf (Holloway, Chatwin & Craig 2001; Jones *et al.* 2020), the Faeroe–Shetland Channel (Hosegood, Bonnin & Van Haren 2004), the St Lawrence River estuary (Bourgault *et al.* 2014), Monterey Bay, CA (Walter *et al.* 2014) and the continental slope of the northern South China Sea (Reeder, Ma & Yang 2011; Ma *et al.* 2016).

Laboratory and numerical studies, to examine NLIW breaking on uniform slopes (Boegman *et al.* 2005), identified three different breaking mechanisms (spilling, plunging and collapsing), based on an internal form of the Iribarren number:

$$Ir = \frac{S}{\sqrt{S_{wb}}}, \tag{1.1}$$

where S is the boundary slope, $S_{wb} = a/\lambda$ is the wave slope, a is the wave amplitude and λ is the wavelength (figure 1).

Aghsaee *et al.* (2010; their figure 6) further classified breaking by performing high-resolution fully nonlinear two-dimensional (2-D) direct numerical simulations

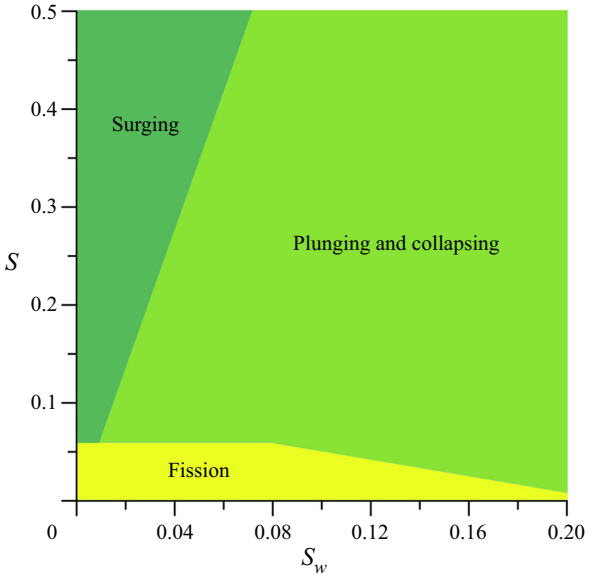

Figure 2. Different breaking mechanism regimes for incident NLIWs, classified according to wave slope (S_w) and bottom slope (S) based on the results by Nakayama *et al.* (2019).

(DNSs) over a wider range of bottom slopes. They categorized breaking of internal solitary waves (ISWs) into four distinct processes (collapsing, plunging, surging and fission) as a function of S and $S_w = a/L_w$, where $L_w = 0.5\lambda$ is the wave half-width. An ISW is an idealized ocean wave, defined as an isolated nonlinear dispersive wave that propagates without changing shape (Lamb 2014); whereas NLIW is a general term that includes ISWs. Sutherland, Barrett & Ivey (2013) combined the results of Aghsaee *et al.* (2010) and Boegman *et al.* (2005) with their own experimental data to generally classify breaking in terms of the Iribarren number. Nakayama *et al.* (2019) performed further three-dimensional (3-D) simulations to show that S and S_w can separate fission and surging breakers, but not collapsing and plunging breakers (figure 2). They introduced a new criterion to classify these two specific breaker types (see their (12)).

Most wave-breaking events (e.g. Oregon shelf, New Jersey shelf, South China Sea) occur on mild slopes ($0.001 < S < 0.01$), where fission is the predominant breakdown process as incident waves of depression change polarity to waves of elevation during shoaling (Shroyer *et al.* 2009; Aghsaee *et al.* 2010; Lamb & Xiao 2014). Fission requires a gradual slope in a large domain, and so has only been computationally modelled over slopes where $S \leq 0.05$ (e.g. Aghsaee *et al.* 2010; Arthur & Fringer 2014, 2016; Lamb & Warn-Varnas 2015; Nakayama *et al.* 2019; Guo *et al.* 2021); typical experimental boundary slopes (e.g. Boegman *et al.* 2005; Sutherland *et al.* 2013) being too short (∼2–6 m) for fission to be observed (table 1; figure 2). Given that Helfrich (1992) had a long flume with a gentle slope ($S = 0.03$; table 1), it is likely that he observed fission, as suggested by Michallet & Ivey (1999).

Fission is the transformation of an ISW into a wave train as a result of a change in the environmental conditions (Boegman & Stastna 2019). In our experiments, this occurs owing to a change in total depth, which causes an incident NLIW of depression to pass through a turning point (figure 1), where the lower fluid layer becomes thinner than the

https://doi.org/10.1017/jfm.2021.1033 Published online by Cambridge University Press

	Name	Bottom slope, S	Flume length (m)	Fluid depth, H (m)	Incident wave / Breaker type
Experimental studies	Southard & Cacchione (1972)	0.1	11	0.4	Sinusoidal internal waves / collapsing
	Wallace & Wilkinson (1988)	0.03, 0.054	18	0.5	ISWs of elevation / transfer to bolus
	Helfrich (1992)	0.034, 0.05, 0.067	18	0.36	ISW of depression / collapsing and fission
	Michallet & Ivey (1999)	0.069, 0.169, 0.214	4.47	0.15	ISW of depression / collapsing and plunging
	Boegman *et al.* (2005)	0.1, 0.15	6	0.29	ISW of depression / collapsing, plunging and spilling
	Boegman & Ivey (2009)	0.145	6	0.29	ISW of depression / plunging
	Sutherland *et al.* (2013)	0.143, 0.417	1.97–6.90	0.43–0.46	ISW of depression / collapsing, plunging and surging
	Moore *et al.* (2016)	0.2	4.88	0.56	Periodic internal wave trains/ collapsing, plunging and surging
	Allshouse & Swinney (2020)	0.176	4	0.4	Isolated internal wave/ surging
	Present study	0.04	18.2	0.4	NLIWs of depression / fission
Field observations	Halpern (1969)	0.005			
	Sandstrom & Elliott (1984)	0.005			
	Holloway (1987)	0.0015			
	Klymak & Moum (2003)	0.007			
	Hosegood *et al.* (2004)	0.017			
	Reeder *et al.* (2011)	0.005, 0.03			
	Richards *et al.* (2013)	0.008, 0.035			
	Ma *et al.* (2016)	<0.017			
	Jones *et al.* (2020)	0.0015, 0.0055			

Table 1. Comparison between boundary slopes used in experimental studies of shoaling NLIWs and observed boundary slopes in the coastal ocean. Note that the experimental slopes are typically orders of magnitude greater than those observed in the ocean, which leads to differing breaking mechanisms in the laboratory compared with the ocean.

upper fluid layer, and leads to fission of the incident wave into a rank-ordered packet of NLIWs of elevation (Grimshaw, Pelinovsky & Talipova 1998; Nakayama *et al.* 2019; Xu & Stastna 2020).

Considering the common gradual slopes in lakes ($\sim$0.01) and coastal oceans ($\sim$0.001; Cacchione, Pratson & Ogston 2002 and table 1), it can be deduced that fission would be the most common breaker type, as shown by field observations (Orr & Mignerey 2003; Shroyer *et al.* 2009; Ma *et al.* 2016). Despite the common occurrence of fission, the limitations of small domains in both experimental and numerical set-ups have resulted in a research focus on steeper slopes and the associated breaking mechanisms (e.g. plunging and collapsing) that are less common in the field (table 1; also see Boegman *et al.* (2005), their table 2). The numerical studies that have been performed on fission have been analytical (Grimshaw *et al.* 1998), 2-D (Aghsaee *et al.* 2010; Xu & Stastna 2020), a 3-D simulation that did not examine a wide parameter space (Arthur & Fringer 2014, 2016) and one that did not provide detailed information about the final stages of shoaling (Nakayama *et al.* 2019).

Shoaling and breaking of internal waves can result in the formation of a bolus (a turbulent vortex with a circulation region within its interior) that progresses along the bed and may become detached from the pycnocline. Boluses may transport mass and bed material upslope in a (quasi-)trapped core (Helfrich & Melville 1986; Helfrich 1992; Venayagamoorthy & Fringer 2007; Vieira & Allshouse 2020). Observations of boluses in the ocean have been reported in field studies (e.g. Klymak & Moum 2003; Carter, Gregg & Lien 2005; Moum *et al.* 2007; Walter *et al.* 2012; Richards *et al.* 2013; Jones *et al.* 2020). Bolus-induced transport influences coastal ecosystems, where dense, cold and nutrient-rich water is transported upslope. This can be critical for the maintenance of coral reefs and kelp forests (Leichter *et al.* 1996), where the cool ambient water reduces coral bleaching (Leichter *et al.* 1996; Goreau *et al.* 2000; West & Salm 2003). Breaking of NLIWs and the resultant formation of boluses can act as a nutrient pump, which supplies the required nutrients to the euphotic zone on the shelf (Sandstrom & Elliott 1984; Bogucki, Dickey & Redekopp 1997; Scotti &Pineda 2004). Boluses may also resuspend and transport sediments upslope (Southard & Cacchione 1972; Bourgault, Kelley & Galbraith 2005; Richards *et al.* 2013; Vieira & Allshouse 2020) with the finer grains transported offshore by the return flow to form an intermediate nepheloid layer (Ivey &Nokes 1989; McPhee-Shaw 2006; Nakayama *et al.* 2012; Pomar *et al.* 2012) and the coarser sediments settling to make bedforms (Karl, Cacchione & Carlson 1986; Reeder *et al.* 2011; Boegman & Stastna 2019). Resuspension and transport can act on settled larvae and cysts, injecting them into the water column and transporting them upslope inside trapped cores (Scotti & Pineda 2004).

The formation of bolus-like flow features has been studied experimentally (Wallace & Wilkinson 1988; Helfrich 1992; Michallet & Ivey 1999; Moore, Koseff & Hult 2016; Allshouse & Swinney 2020) and numerically (Venayagamoorthy & Fringer 2007; Aghsaee *et al.* 2010; Arthur & Fringer 2014, 2016; Bourgault *et al.* 2014; Vieira & Allshouse 2020). Wallace & Wilkinson (1988) observed the formation of one bolus for each incident wave, as the final stage of shoaling of ISWs of elevation over gentle slopes ($S = 0.03,\ 0.054$; table 1). In comparison, Helfrich (1992) observed the formation of several boluses (3–10; their figure 9) during ISW shoaling on uniform slopes (table 1). Michallet & Ivey (1999) also studied breaking of NLIWs of depression on steep slopes and observed a single bolus after breaking (table 1). The most comprehensive laboratory study (Moore *et al.* 2016) observed bolus formation as the final stage of periodic internal wave train shoaling in a quasi-two-layer system on a uniform slope ($S = 0.2$; table 1). They categorized boluses

into four types, based on the breaking mechanism (collapsing, plunging and two types of boluses for surging). They did not observe fission, as their slope was too steep.

Aghsaee *et al.* (2010) performed 2-D DNS of bolus generation from collapsing, plunging and surging breakers. They proposed that ISWs of elevation, with trapped cores, are the final stage of shoaling during fission. Bourgault *et al.* (2014) and Masunaga *et al.* (2017) simulated the 2-D field-scale sediment movement and resuspension by boluses from fission and surging breaking of internal waves, respectively. These were in good visual agreement with field observations. Venayagamoorthy & Fringer (2007) simulated propagation of boluses over slope-shelf topography and concluded that 2-D simulations could accurately reproduce bolus dynamics. Three-dimensional boluses were simulated to occur from fission by Arthur & Fringer (2014) and were strikingly similar in structure to the observations of Helfrich (1992) for the same wave amplitude and bathymetric slope. More recently, Vieira & Allshouse (2020) performed numerical simulations that found the thickness of the pycnocline influenced the bolus characteristics resulting from surging of internal waves over steep slopes ($S = 0.105 - 0.231$). This was validated experimentally by Allshouse & Swinney (2020) who observed three ball, hook and sliver boluses to evolve from surging breakers.

Given the lack of experimental data on shoaling of boluses generated by fission of NLIWs, there is a need for further laboratory-based research on this topic. The objectives of the present study are to characterize experimentally the final stage of breaking by fission, to parameterize bolus dynamics (number of boluses, bolus size, propagation distance) in terms of readily measurable incident wave parameters and to compare boluses generated from fission to those generated by other mechanisms. This knowledge will help oceanographers better understand NLIW shoaling and breaking, better choose mooring sites, better interpret the observed data, and will help validate and improve numerical simulations at both the laboratory and field scales.

2. Materials and methods

2.1. *Theoretical background*

To parameterize our results and compare our data with existing parameterizations, we present the relevant theoretical background. In stratified lakes and oceans, when the pycnocline is much thinner than the total depth $H = h_1 + h_2$, a density stratified fluid can be approximated as a quasi-two-layer system with a lower layer depth h_2 and density ρ_2 which is overlaid by an upper layer with depth h_1 and density ρ_1.

Although many of their waves were strongly nonlinear (e.g. $a > h_1$ Stanton & Ostrovsky (1998); $a/h_1 > 0.22$, Cui, Dong & Wang 2021), Helfrich (1992) and Aghsaee *et al.* (2010) parameterized their results in terms of the weakly nonlinear Korteweg–de Vries (KdV) equation for an inviscid fluid under the Boussinesq approximation (Osborne & Burch 1980; Apel 2002; Ostrovsky & Stepanyants 2005):

$$\eta_t + c_0\eta_t + \alpha\eta\eta_x + \beta\eta_{xxx} = 0, \tag{2.1}$$

$$\alpha = \frac{3c_0}{2}\frac{h_1 - h_2}{h_1 h_2}, \quad \beta = \frac{c_0}{6}h_1 h_2, \tag{2.2a,b}$$

$$c_0 = \sqrt{\frac{g' h_1 h_2}{H}}, \tag{2.3}$$

$$c = c_0 + \left(\frac{\alpha a}{3}\right), \tag{2.4}$$

$$\lambda_{KdV} = \sqrt{\frac{12\beta}{\alpha a}}, \tag{2.5}$$

$$\gamma = \frac{|\alpha| a}{c_0} = \frac{3}{2} a \frac{|h_1 - h_2|}{h_1 h_2}. \tag{2.6}$$

Here η is the vertical displacement of the pycnocline, α is the nonlinearity coefficient, β is the dispersion coefficient, c_0 is the linear long-wave speed, c is the nonlinear wave phase speed, a is the wave amplitude (negative for a wave of depression), $g' = g(\rho_2 - \rho_1)/\rho_2$ is the reduced gravity owing to stratification, λ_{KdV} is the characteristic length scale of a KdV-type solitary wave and γ is the non-dimensional nonlinearity parameter (Boegman *et al.* 2005).

The applicability of weakly nonlinear KdV theory to characterize our observations was assessed by an a/h_1 criterion applicable for density stratifications $0.11 < h_1/h_2 < 0.43$ (Cui *et al.* 2021; their table 5). In KdV theory, waves of depression exist only when $h_1 < h_2$, causing fission to occur as the wave passes through the turning point where the nonlinearity coefficient vanishes ($\alpha \to 0$). Equations (2.2) and (2.5) show a and α to have the same sign and, consequently, the change to a wave of elevation as $\alpha > 0$ whence $h_1 > h_2$ after the turning point (Grimshaw *et al.* 1998). We differentiate our lab-observed waves as narrow or broad-crested according to $0.1 < \gamma < 3$, or equivalently $a < (h_2 - h_1)/2$, from (2.6). Aghsaee *et al.* (2010) applied this criterion to show that the majority of ISWs observed in the field were narrow crested.

To calculate the observed NLIW half-width, we followed Michallet & Ivey (1999):

$$L_w = \frac{c}{a} \int_{t_0}^{t_1} \eta(t)\, \mathrm{d}t, \tag{2.7}$$

where the corresponding wave period is

$$T = \frac{2L_w}{c}. \tag{2.8}$$

We compared our results with the parameterizations introduced by Hult, Troy & Koseff (2010) and Moore *et al.* (2016). These embody both the incident wave and ambient fluid properties, which are readily measurable in the field. They include wave steepness (ka), wave Reynolds number (Re) and wave Froude number (Fr):

$$ka = \frac{2\pi a}{\lambda}, \tag{2.9}$$

$$Re = \frac{\omega a^2}{\upsilon}, \tag{2.10}$$

$$Fr = \frac{\omega a}{\sqrt{g'_c H'}}, \tag{2.11}$$

where $k = 2\pi/\lambda$ is the wavenumber, $\omega = 2\pi/T$ is the wave frequency, $g'_c = 2g(\rho_2 - \rho_1)/(\rho_2 + \rho_1)$ is the reduced gravity for this set of equations, $H' = h_1 h_2/H$ in an equivalent depth and υ is the kinematic viscosity.

2.2. *Experimental set-up and measurement techniques*

The experiments were conducted in the Queen's University Internal Wave Flume, a glass-walled rectangular wave flume (figure 3, 18.2 m long, 0.75 m wide and 0.58 m deep).

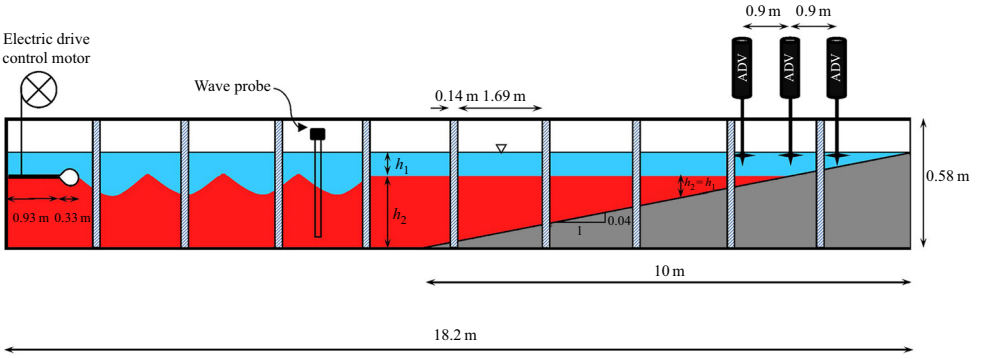

Figure 3. Schematic of experimental set-up. Periodic NLIWs of depression are generated within the two-layer fluid by flapping the wave paddle with an electric motor connected through an eccentric drive shaft. The upper fluid layer is fresh water and the lower fluid layer is saline. See table 2 for a list of the experimental parameters.

A planer Perspex slope ($S = 0.04$) extended upward from the bed to a height of 40 cm at the end wall. This was the mildest practical slope that could be installed in the flume and expected to generate fission (figure 2). This slope was close to the oceanic case ($S = 0.035$; table 1), where Richards *et al.* (2013) observed boluses. At the other end of the flume, an aluminium flapping airfoil-type horizontal wave paddle (Thorpe 1978; Nakayama & Imberger 2010) was installed to generate internal waves with different amplitudes and periods. The wave paddle was as wide as the flume and consisted of a 33 cm long airfoil connected with a piano hinge to a 93 cm long flapping plate (figure 3). The plate was driven by an electric motor connected with an eccentric drive shaft.

The flume was filled to a total depth of $H = 40$ cm using two different layer densities ($\rho_2 = 1020$ or $1040\,\mathrm{kg\,m^{-3}}$) and heights ($h_2 = 25$ or 30 cm) chosen based on the limitations of the wave paddle (size and practical movement) and also the wave gauge (operational range in saline water). The density stratification was prepared by adding fresh water to the flume to the desired depth (h_2), which was measured with transparent ruler tape (± 2 mm), and then adding salt (Cargill Calcium Magnesium Free) to reach the desired density (ρ_2), which was measured with a hydrometer (Fisherbrand™ 11555G; $\pm 2\,\mathrm{kg\,m^{-3}}$). The lower layer was seeded with food dye to enable flow visualization. Fresh water ($\rho_1 = 998\,\mathrm{kg\,m^{-3}}$) was slowly added over the lower layer, using a floating sponge to minimize mixing between the two layers, until the appropriate upper layer thickness (h_1) was achieved. This method created a density stratification with a thicker lower saline layer underlying a thinner fresh layer separated by a thin pycnocline $\delta \approx 2$ cm $\pm$ 2 mm (Troy & Koseff 2005), commonly known as a 'quasi two-layer' stratification. The stratification profile can be theoretically reproduced as a hyperbolic tangent function and supports NLIWs of depression, which is typical oceanic stratification (Helfrich & Melville 2006; Jackson, Da Silva & Jeans 2012; Allshouse &Swinney 2020).

The wave paddle was positioned at the interface between the two fluid layers. To generate NLIWs of depression, the plate was flapped downward at the end wall to a desired depth (approximate wave amplitude) and then driven upward to the horizontal (i.e. the location of the quiescent density interface) using the electric motor. Measured wave amplitudes were typically 70 % of the flapping plate displacement along the end wall. Periodic movement of the paddle forced both the upper and lower layers generating a continuous train of NLIWs of depression. The wave amplitude was increased, in successive experiments, until the paddle movement created excessive localized mixing. In coastal regions, observations of ~3–11 NLIW packets (Jackson 2007), with ~10 rank-ordered NLIWs in each packet

Run	a (m)	ρ_2 (kg m^{-3})	h_2 (m)	γ	T (s)	c (m s^{-1})	L_w (m)	S_w	ka	Re	Fr
1	−0.024	1020	0.30	0.24	26.3	0.136	1.790	0.013	0.042	137	0.045
2	−0.045	1020	0.30	0.45	16.6	0.145	1.206	0.037	0.117	764	0.134
3	−0.028	1040	0.30	0.28	19.2	0.188	1.812	0.015	0.048	256	0.052
4	−0.045	1040	0.30	0.45	12.2	0.198	1.206	0.037	0.117	1045	0.133
5	−0.055	1020	0.25	0.22	30.1	0.151	2.277	0.024	0.076	631	0.081
6	−0.083	1020	0.25	0.33	22.9	0.156	1.791	0.046	0.146	1890	0.161
7	−0.055	1040	0.25	0.22	22.0	0.207	2.277	0.024	0.076	863	0.081
8	−0.083	1040	0.25	0.33	17.2	0.214	1.836	0.045	0.142	2524	0.156

Table 2. Experimental parameters, where a is the wave amplitude (negative means wave of depression), ρ_2 is the lower layer fluid density, h_2 is the lower layer thickness, γ is non-dimensional nonlinearity parameter (2.6), T is the wave period (2.8), c is the nonlinear wave phase speed (2.4), L_w is the wave half-width (2.7), S_w is the wave slope, ka is the wave steepness (2.9), Re is the wave Reynolds number (2.10) and Fr is the wave Froude number (2.11) (the boundary slope $S = 0.04$ and the total height $H = 0.4$ cm are constant for all the tests).

(e.g. Stanton & Ostrovsky 1998; Shroyer *et al.* 2009; Zulberti, Jones & Ivey 2020), are more common than lone solitary waves. Therefore, we followed the approach of Wallace & Wilkinson (1988), Helfrich (1992) and Moore *et al.* (2016) and generated periodic trains of NLIWs. This also facilitated piece-wise measurement of the velocity profile over successive wave shoaling events.

The applicability of KdV theory to describe our experimentally generated waves was not known *a priori*. The NLIW half-width was expected to scale with the length of the flapping plate and, for KdV waves, would be coupled to the wave amplitude according to (2.5). Therefore, the wave amplitude was first set by the vertical excursion of the flapping plate and then (2.5) was applied to compute the wavelength, which was taken as $\lambda \approx 9\lambda_{KdV}$ following the observations by Aghsaee & Boegman (2015). Using this modified wavelength, the wave period (2.8) was then determined and set as the period of rotation of the motor. Regardless of whether or not the NLIWs are accurately described by KdV theory, similar to lone waves formed by lock release, the resultant periodic NLIWs will evolve to their natural form once generated by an interfacial disturbance.

For this study, eight experiments with different wave amplitudes and density stratifications were performed (table 2). To measure a and T, a capacitance-type surface wave probe was customized to measure internal waves, using foam insulation to prevent spurious oscillations of the free surface from contaminating the internal wave signal (Wallingford HRIA-1018). The wave probe was installed 3 m downstream from the wave paddle (figure 3). The flow was visualized with backlight from fluorescent tubes illuminating translucent Perspex diffusing sheets, and recorded with three high-definition video cameras, two Canon 650D recorded the upslope wave propagation from the side, and a Canon VIXIA HV30 recorded the overhead plan view. The physical characteristics of the observed phenomena were measured with transparent ruler tape affixed to the flume and by digitizing the videos in Grapher software. The bolus propagation distances were recorded manually during each experiment.

Time series of velocity profiles within the boluses were recorded with three acoustic Doppler velocity profilers (ADVPs; Nortek Vectrino II; 1 mm s^{-1} precision and ±5 % measurement error). One ADVP was positioned where the pycnocline intersects the slope (interaction point; figure 1) and the other two ADVPs were positioned both 90 cm upstream and downstream of the interaction point (figure 3). All three ADVPs were set to measure

3-D velocity profiles at 50 Hz over a 3 cm vertical profile (4 cm to 7 cm from the ADVP probe) with 1 mm resolution. At the beginning of each test, the ADVPs were 6 cm above the bottom, which caused 1 cm of the profile to be lost beneath the bed, so as to locate the region of maximum signal-to-noise ratio (SNR) or 'sweet spot' directly at the bed and minimize acoustic reflection. The SNR was also increased by local seeding with talcum powder (Ahmari 2013). During each experiment, the velocity profile was measured by iteratively moving the ADVP vertically through the water column on pointer gauges (± 0.1 mm). At each depth, five consecutive NLIWs of depression were measured (from five rotations of the motor) with the middle wave being chosen to be representative of an NLIW in a shoaling packet. The first and last waves had different characteristics than those in the middle, consistent with the observations by Wallace & Wilkinson (1988), Helfrich (1992) and Moore *et al.* (2016).

A sensitivity analysis showed that the measurements were invariant for packets consisting of ten consecutive waves. After each cycle of five waves, the ADVPs were moved 2 cm upward and the procedure was repeated to capture new velocity profiles, with 1 cm overlap, until the ADVP reached the surface. A maximum of seven runs was required to capture the entire velocity profile (for $h_2 = 0.25$ m; table 2). Diapycnal mixing from shoaling boluses was observed to be minimal over the very long pycnocline (16.25 m to 18.5 m; figure 1), consistent with numerical simulations by Arthur & Fringer (2014), (2016). Experiments were terminated before appreciable variation in the bolus characteristics or thickening of the pycnocline was observed (e.g. Ivey & Nokes 1989; Michallet & Ivey 1999; Boegman & Ivey 2012).

Only velocity data with average correlation $> 60\,\%$ and SNR > 15 dB were retained for analysis (McLelland & Nicholas 2000; Nikora & Goring 2000; Chanson 2008). The data were despiked using a phase-space thresholding technique (WinADV 2.031) and the final profiles were stitched together in Matlab. As the flow was unsteady, mean velocity profiles $(\bar{U}, \bar{V}, \bar{W})$ were obtained by applying a low-pass filter to the instantaneous velocity data (u, v, w) with a spectral cutoff between peaks associated with the NLIWs and small-scale turbulence (Aghsaee & Boegman 2015). The velocity signals were then decomposed into mean and turbulent components using a Reynolds decomposition (e.g. $u = \bar{U} + u'$). We were unable to measure the velocity profile within 4 cm of the free surface and 0.5 cm of the bed, owing to the probe configuration and SNR limits close to the solid boundary, respectively (Chanson 2008; Aghsaee & Boegman 2015).

3. Results

3.1. *Flow field*

Periodic movement of the paddle generated a train of NLIWs of depression that travelled toward the slope passing through the wave probe (figure 4). The wavelength (table 2), measured by the wave probe (figure 4 and (2.7)) was larger than the characteristic KdV wavelength from (2.5); $\lambda = 2L_w \approx 7\lambda_{KdV}$. It is well known that for large amplitude NLIWs, the wavelength from (2.5) is too narrow (Wallace & Wilkinson 1988; Boegman & Stastna 2019). For example, field observations show $\lambda \approx 3.6\lambda_{KdV}$ (Holloway 1987; Boegman *et al.* 2003) and lab experiments show $\lambda \approx 9\lambda_{KdV}$ (Aghsaee & Boegman 2015). Therefore, our NLIWs were not well described by KdV theory (e.g. when $a > h_1$, Stanton & Ostrovsky 1998). We found $a/h_1 > 0.22$ (Cui *et al.* 2021), which confirmed that weakly nonlinear KdV theory was not applicable to our observations and extended KdV would be more appropriate.

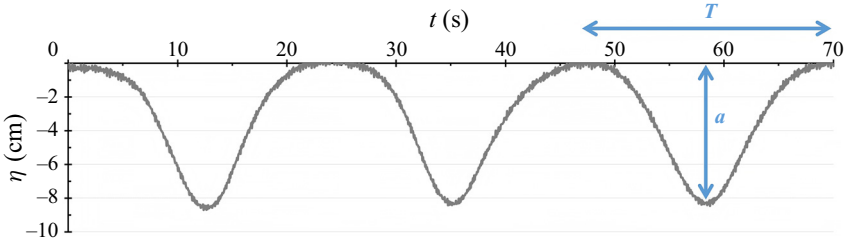

Figure 4. Time series of the pycnocline displacement (η) for the run 6 recorded by the wave probe. The resultant wave amplitude (a) and wave period (T) are shown.

The non-dimensional nonlinearity parameter (2.6) confirms that all the observed waves were narrow crested as $0.1 < \gamma < 3$ (table 2). Moreover, in all the experiments, $L_w < 0.35L_i$, where L_i is the pycnocline length above the slope (figure 1). Therefore, a positive tail was expected to form behind the rear face of the wave of depression over the slope (Aghsaee *et al.* 2010). Shear-induced breaking was not observed prior to shoaling, as confirmed by $a < 2.24\sqrt{h_1\delta}(1 + \delta/h_1)$ (Fructus *et al.* 2009).

3.2. *Wave shoaling and bolus formation*

When the train of NLIWs of depression shoaled over the mild slope, each incident NLIW of depression (figure 5*b*; blue arrow) degenerated through fission into one or two NLIWs of elevation as it passed through the turning point (figure 5; green line). In this process, the leading face of the NLIW of depression became elongated, parallel to the slope and the rear face steepened. A positive tail (Aghsaee *et al.* 2010) formed behind the rear face of the wave, which eventually evolved into one or more NLIWs of elevation (figure 5*d*; blue arrow), as in the observations by Orr & Mignerey (2003) and Ma *et al.* (2016).

In figure 5 (run 2, table 2), for each NLIW of depression, there was only one NLIW of elevation after the turning point. Each NLIW of elevation then transformed into a bolus at the 'birth point' (figure 5*g*; blue arrow), which was between the turning point and the interaction point (figure 1; see also §§ 4.1 and 4.2). The boluses propagated upslope, decreasing in size until they degenerated (figure 5*k*; blue arrow). Each bolus preceded the next bolus formed from the subsequent NLIW of depression in the train (bolus downslope of the blue arrow in figure 5*k*). There was no evidence of reflection, as in the observations by Haury *et al.* (1979).

The transformation from an NLIW of elevation into a bolus is difficult to observe with discrete oceanographic moorings (Jones *et al.* 2020); this transformation is shown in figure 6 (run 6; table 2). The NLIW of elevation formed after the turning point, which is outside the field of view (figure 6*b*), and progressed upslope as the rear face steepened (figure 6*c*). At the bolus birth point (figure 6*d*; blue arrow), the rear face steepness was maximum and shear instabilities, in the form of Kelvin–Helmholtz billows, were observed to develop through the density interface, particularly along the rear face. The bolus formed as a turbulent vortex, with a thin trailing return flow of lower layer fluid attached to the pycnocline (§ 4.1). The bolus moved upslope while gradually deceasing in size until it degenerated (run 2, figure 5). The boluses were all similar in shape (e.g. Wallace & Wilkinson 1988; their figure 7); hook- and sliver-type boluses simulated on thicker pycnoclines and steeper slopes were not observed (Vieira & Allshouse 2020).

For some experiments, two boluses formed from each incident NLIW of depression (§ 4.3.4); thin return flow in the lower layer, both in front and behind, connecting the

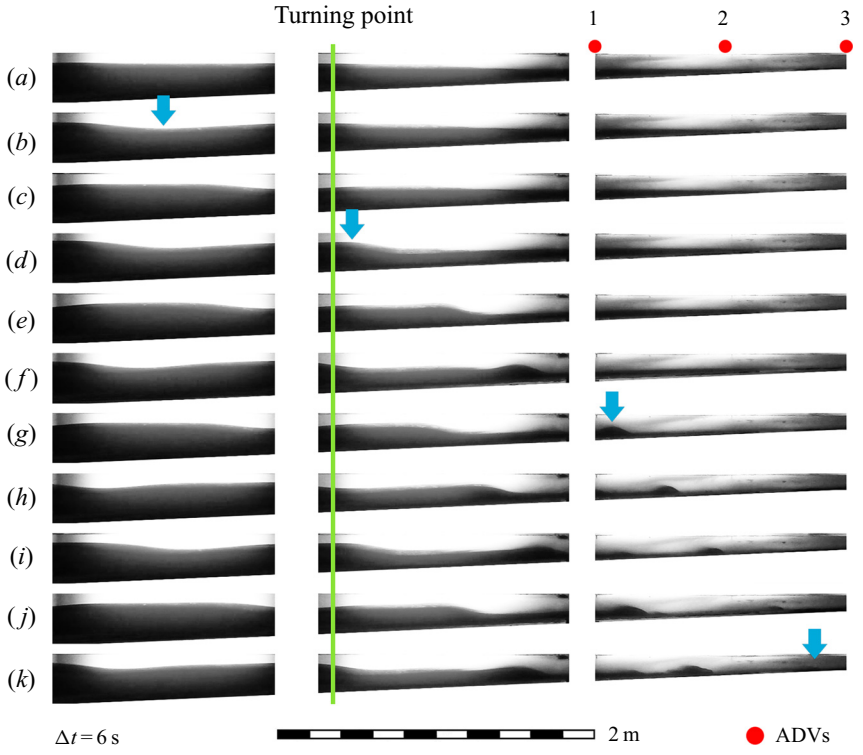

Figure 5. Snapshots in time for run 2 (each row represents a time step), which show fission for a typical NLIWs of depression over a mild slope and bolus formation when there is one bolus for each incident NLIW of depression. The blue arrows in *b*, *d*, *g* and *k* show the incident NLIW of depression, the evolving NLIW of elevation after the turning point, the bolus and the point where the bolus has completely dissipated, respectively. Time period between snapshots is $\Delta t = 6$ s and the locations of the ADVPs are shown with red dots. All three image panels are acquired simultaneously with the same camera.

boluses (§ 4.3.3). As an example of this, figure 7 shows snapshots for run 1 (table 2), where an NLIW of depression has passed the turning point. The first NLIW of elevation formed behind the rear face of the incident wave of depression, which had steepened (figure 7*b*). The first NLIW of elevation evolved into a bolus (as for the lone bolus in figure 6*d*) but remained attached to the pycnocline with a tongue of lower layer fluid (figure 7*d*; blue arrow). As the first bolus propagated away, a second NLIW of elevation formed where the rear face continued to shoal (figure 7*e*; orange arrow). A second bolus was similarly generated after forming another positive tail (figure 7*f*; green arrow). The creation of more boluses was prevented by elongation of the leading face of the next NLIW of depression in the wave train (figure 7*h*).

The waves of elevation, generated by fission, were rank-ordered and there was no evidence of interaction between the first wave of elevation (or bolus) generated by a trailing wave of depression and the last wave of elevation (or bolus) generated by the preceding wave of depression. Each bolus completely degenerated before the arrival of the trailing bolus (figure 7 and supplementary movie S1 available at https://doi.org/10.1017/jfm.2021.1033). These observations (figure 7) are consistent with the simulations by Arthur & Fringer (2014) (their figure 18).

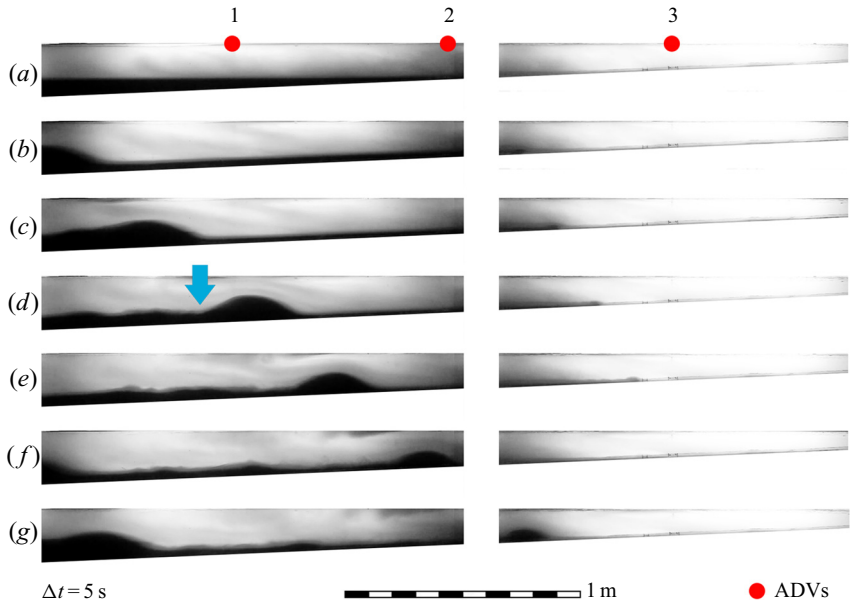

Figure 6. Snapshots in time for the run 6 which show typical transformation of an NLIW of elevation to a bolus when there is one bolus for each incident NLIW of depression. The blue arrow shows the location where the rear face of the NLIW of elevation reaches maximum steepness, and shear instability in the form of Kelvin–Helmholtz billows forms through the rear face. We consider this to be the bolus birth point. Thereafter, the bolus progresses upslope, decreasing in size until it degenerates. The time interval between snapshots is $\Delta t = 5$ s and the locations of the ADVPs are shown with red dots. Each image panel is acquired with a different camera.

3.3. *Bolus instability*

Shear instability was observed through the bolus pycnocline and lobe-cleft instability at the leading edge (Simpson 1972; Venayagamoorthy & Fringer 2007; Arthur & Fringer 2014). The instabilities through the pycnocline, particularly near the crest and through the rear face, formed from strong shear in the parallel flow (§ 4.1; movie S3 in the supplementary material). At times the instabilities were in the form of Kelvin–Helmholtz billows, for example at the front of the bolus (just above the nose) in figure 8(*a*). Similarly, Jones *et al.* (2020) also observed shear instability through the rear face of near-bed NLIWs of elevation in the ocean.

A linear stability analysis (Gímez-Giraldo *et al.* 2008; Smyth, Moum & Nash 2011; Bouffard, Boegman & Rao 2012), using a tanh density profile and the mean observed horizontal velocity profile (figure 8*a*, trailing the bolus), showed peak growth of mode-one instabilities to be centred at a wavelength of 0.6 cm. This wavelength is consistent with the size of the small-scale overturns in figure 8(*a*) (figure S1).

A plan view (figure 8*b*, yellow arrow) shows the lobe-cleft instability of the leading face (Härtel, Carlsson & Thunblom 2000; Venayagamoorthy & Fringer 2007; Xu, Subich & Stastna 2016; Jones *et al.* 2020). There is no return flow toward the leading bolus (figure 8*b*, yellow arrow), which is visually similar to a shoaling ISW of elevation or gravity current (e.g. Simpson 1972, their figure 11; Härtel *et al.* 2000, their figure 1; Xu *et al.* 2016, their figure 5). The irregular pattern of the leading edge (figure 8*b*; green arrow) shows that the lobe-cleft instability occurred during the presence of a return flow (before degeneration of the leading bolus), as simulated by Xu *et al.* (2016). The three-dimensional structure of

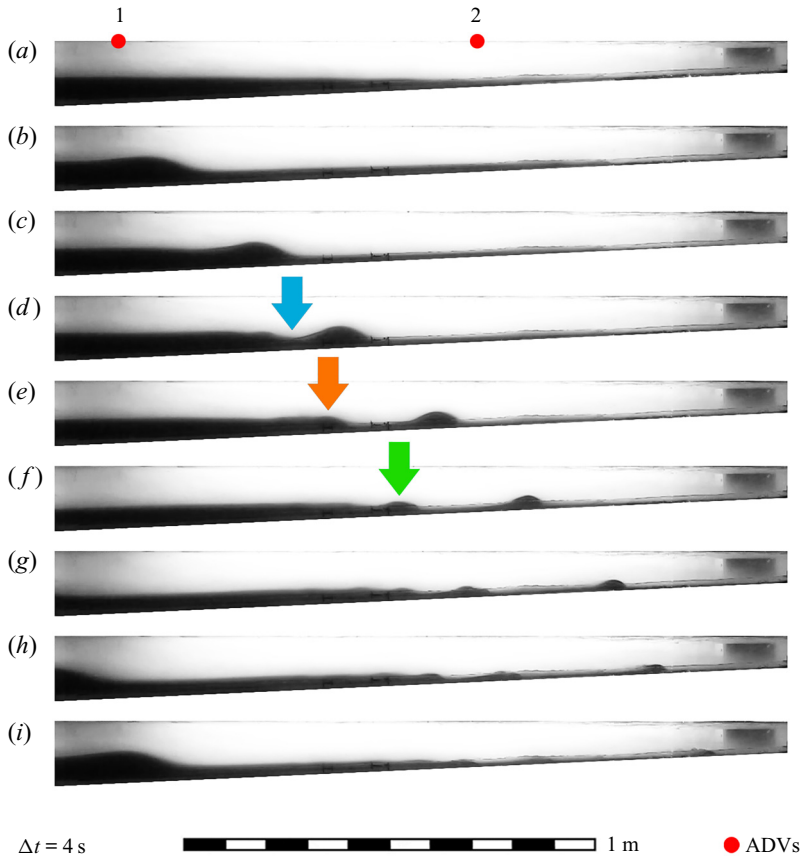

Figure 7. Snapshots in time for run 1 which show typical bolus formation mechanism when there are two boluses for each incident NLIW of depression. The blue arrow shows the tongue of the lower layer fluid attaching the first bolus to the pycnocline. The orange arrow shows the second NLIW of elevation and the green arrow shows the second bolus (see supplementary movie S1). The time interval between snapshots is $\Delta t = 4$ s and the locations of the ADVs are shown with red dots. The third ADVP is outside the field of view.

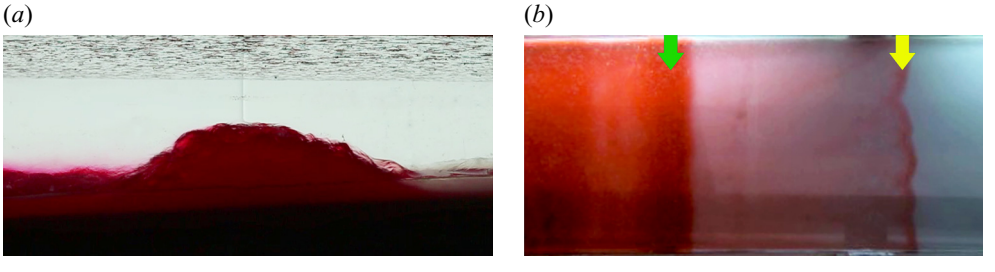

Figure 8. Images showing run-up of a bolus after its formation (run 4). The bolus is travelling from left to right in the upslope direction. (*a*) Side view (see supplementary movie S2), (*b*) top view of two boluses as indicated by arrows: the green arrow shows the top view of the bolus in panel (*a*); the yellow arrow shows the preceding bolus during its final stage of shoaling as it degenerates (see supplementary movie S3). In this run, there is one bolus for each NLIW of depression. The bolus in panel (*a*) has a height of ∼4 cm and the smaller-scale shear instabilities have length scales of ∼1 cm.

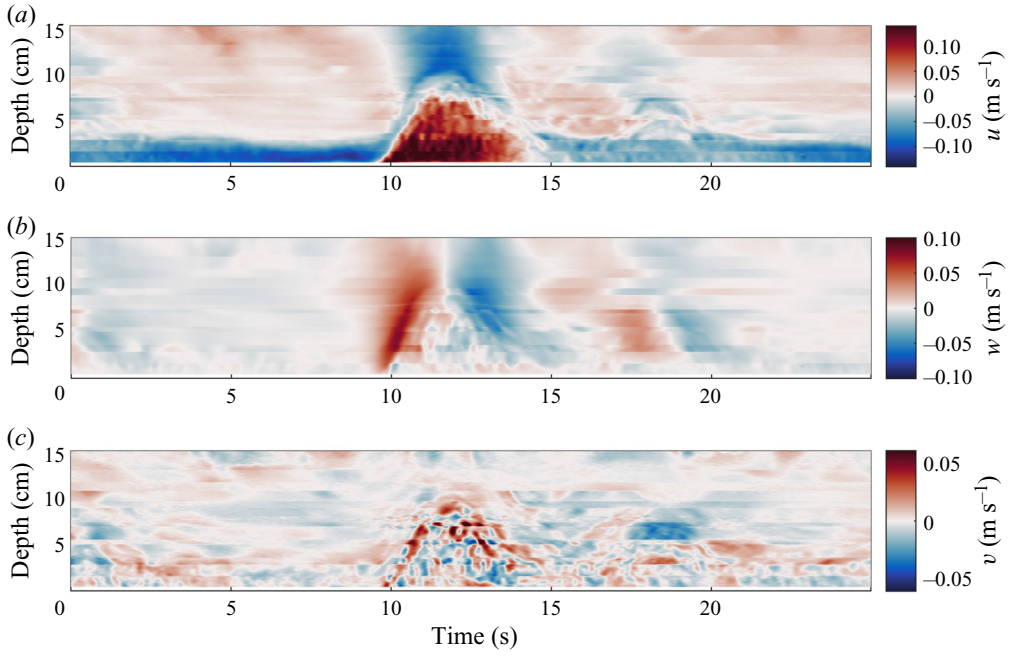

Figure 9. Hovmöller diagram of instantaneous velocity profiles for a bolus in (*a*) the streamwise direction (*u* component), (*b*) the vertical direction (*w* component) and (*c*) the spanwise direction (*v* component) for run 8 (table 2) as captured by the first ADVP. Measured data within 5 mm of the bed have been removed because of poor signal-to-noise ratio and correlation from acoustic reflection of the bottom. In all the experimental data, this is the largest bolus that is recorded with the strongest velocities.

the lobe-cleft instability is evident in our observations, with finite-amplitude features that are long in the streamwise direction (e.g. velocity structure in figure 9*b*) and short in the spanwise direction (e.g. density field in figure 8*b*), as identified by Xu *et al.* (2016; see their figure 7). Lobe-cleft instability has also been observed in oceanographic observations of shoaling NLIWs of elevation (Jones et al 2020).

A strong down-draft of lower layer fluid, near the bed, occurred during the progression of the bolus and diapycnal mixing across the pycnocline was weak, which suggested continued mass flux to the lower layer may be more important than diapycnal mixing across the pycnocline in regulating bolus progression and degeneration. This has implications for irreversible vertical flux of sediments, nutrients and buoyancy along coastal margins (Sandstrom & Elliott 1984; Helfrich 1992; Boegman & Stastna 2019).

3.4. *Velocity field*

The velocity profiles from the three ADVPs, during the eight experiments, captured boluses with different sizes and velocity magnitudes, yet they were qualitatively similar. As an example, figure 9 shows time series of the ADVP-observed instantaneous velocity profiles (*u,w,v*) during the passage of the largest observed bolus (run 8; first ADVP). When the bolus formed, it was preceded by a thin downslope lower-layer flow (figure 9*a*; $t = 0$–9 s; also see figure 8*a* and supplementary movie S3), which formed either from the elongated leading face of the first incident NLIW of depression or the trailing edge of the preceding bolus. When the bolus passed the ADVP, there was an upslope flow of lower layer fluid inside the bolus and a downslope flow of the upper layer fluid above

(figure 9*a*; $t = 9$–14 s). The flow along the leading face of the bolus was upward (figure 9*b*; $t = 9$–12 s) and was downward flow at the rear face (figure 9*b*; $t = 12$–15 s). Spanwise flow within the bolus core was evident, but was strongest through the pycnocline (figure 9*c*; $t = 10$–15 s); which indicated the presence of 3-D instability, particularly along the rear face (e.g. figure 8*a*).

After the bolus passed, a thin downslope return flow (e.g. figure 8 and supplementary movie S3) was also observed (figure 9*a*; $t = 15$–25 s). This drained the dense fluid inside of the bolus to the lower layer or toward the trailing bolus. These velocity fields (figure 9) are consistent with those observed by Richards *et al.* (2013; their figure 9); although they were unable to capture velocity profiles close to the bottom (<1 m above the bed); potentially not resolving a return flow. The size and velocity magnitude, associated with the boluses, decreased as they propagated upslope (figure S2). The fluctuating velocity components were roughly one-tenth the magnitude of the instantaneous components and were elevated within the bolus and along its boundary, which indicated active turbulence (figure S3).

4. Discussion

4.1. *Difference between a NLIW of elevation and a bolus*

Here, we propose that a comparison of the velocity fields can be used to differentiate NLIWs of elevation and boluses. Shoaling NLIWs of elevation have been investigated in the literature (e.g. Stastna & Lamb 2008; Carr & Davies 2010; Xu *et al.* 2016), but their dynamics after generation through fission of an NLIW of depression and the difference between an NLIW of elevation and a bolus remain comparatively uninvestigated in the laboratory. Stastna & Lamb (2008) and Carr & Davies (2010) considered propagation of an ISW of elevation over a horizontal bed, while Wallace & Wilkinson (1988) and Xu *et al.* (2016) considered shoaling over a planar slope and a small-amplitude shelf, respectively. Wallace & Wilkinson (1988) proposed that internal waves of elevation steepened over the slope until they became unstable and eventually overturned transforming into a bolus with instabilities at the crest. Each bolus moved upslope decreasing in size as it degenerated. Carr & Davies (2010) reported three wave types and observed shear instability through the pycnocline for one of them. Arthur & Fringer (2014) simulated the final stage of shoaling, for fission, to be a train of rank-ordered solitary waves of elevation (boluses). Xu *et al.* (2016) simulated the start of lobe-cleft instability at the nose of the wave and shear instability in the form of Kelvin–Helmholtz billows through the rear-wave face during the shoaling over the shelf, but as with Carr & Davies (2010), they did not call these boluses. In the present study, our observations after the turning point were very similar to those of Wallace & Wilkinson (1988) (figure 6).

We compared the velocity fields for an NLIW of elevation and two boluses (figure 10) from run 1 (table 2). Both boluses formed from fission of one incident NLIW of depression; however, the second NLIW of elevation was not captured by the first and second ADVPs (figure 7). In this run, the boluses did not propagate to the third ADVP (figure 7*i*). Therefore, the NLIW of elevation (figure 10*a*,*c*,*e*) transformed into the first bolus (figure 10*b*,*d*,*f*; bolus on the left). The bolus velocity signatures (figure 10*b*,*d*,*f*) were qualitatively similar to the already investigated bolus from run 8 (figure 9*a*–*c*). However, the velocity signature associated with the NLIW of elevation (figure 10*a*,*c*,*e*) was distinct from those arising from the boluses. The u velocity (figure 10*a*,*b*) had a return flow in the lower layer behind the boluses (figure 10*b*, $t = 8$–13 s and $t = 15.5$–20 s) that was not present for the NLIW of elevation (figure 10*a*, $t = 14$–20 s). This is in agreement with the simulations of NLIWs of elevation by Xu & Stastna (2020; their figure 2*a*). The v

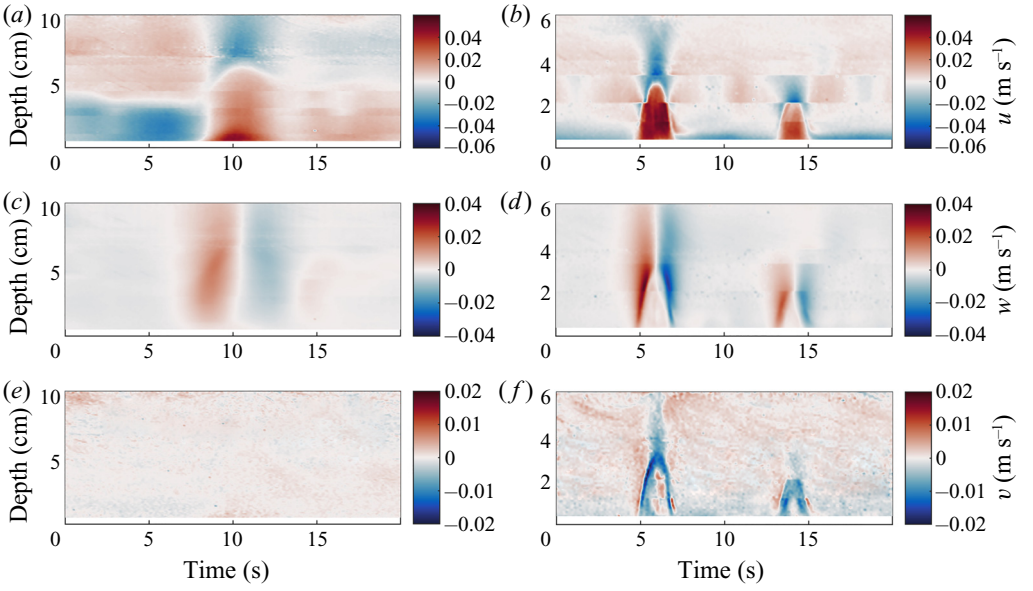

Figure 10. Hovmöller diagram showing contrasting instantaneous velocity profiles for an NLIW of elevation and two boluses. Panels (*a*,*b*), (*c*,*d*) and (*e*,*f*) show the streamwise (*u* component), vertical (*w* component) and spanwise (*v* component) velocity components, respectively, for the NLIW of elevation (left column)/boluses (right column). These data are for run 1 as captured by the first and second ADVPs. The first bolus forms from the shown NLIW of elevation, whereas the second bolus forms from the trailing NLIW of elevation (not shown). Both NLIWs of elevation occur through fission of the same incident NLIW of depression. See figure 7 and supplementary movie S1.

velocity (figure 10*e*,*f*) showed striking spanwise flow for the case with boluses (figure 10*f*, $t = 5$–7 s and $t = 13.5$–15 s), which was not observed in the NLIW of elevation (Hosegood *et al.* 2004). These instantaneous velocities (figure S2) were maximum around the bolus edge, owing to the instabilities in the pycnocline.

The thin region of three-dimensionalization $< \sim 1$ cm (figure 10*f*) is consistent with the wavelength of the most unstable mode (0.5 cm) from a linear stability analysis (figure S4). The size of our instabilities was likely limited by the large density difference across the pycnocline (20–40 kg m^{-3}) in the present experiments, relative to the smaller density gradients in oceanic observations (Moum *et al.* 2003), which would allow for growth of larger instabilities relative to the wave/bolus height.

The current speed inside the first bolus (*u* and *w*; figure 10*b*,*d*) was greater than in the initial NLIW of elevation (*u* and *w*; figure 10*a*,*c*), even though the bolus was smaller and the data were captured 0.9 m further upslope. Considering the reduction in bolus size and velocity magnitude during propagation over the slope (figure S2), it can be surmised that the peak in *u* and *w* velocity components occurred at the bolus birth point.

4.2. *Bolus formation*

The bolus formation mechanism for shoaling internal waves on a slope depends on the wave form (depression versus elevation). From our results and Moore *et al.* (2016), for an incident NLIW of depression, bolus formation depends on the breaker type (fission, collapsing, plunging and surging). However, for an ISW of elevation, Wallace & Wilkinson (1988) proposed that the structure of the bolus was independent of the breaking mechanism and only determined by the inclination of the slope.

The steep-slope boluses, observed by Moore *et al.* (2016), consisted of a vortex with a mixed breaking region that was pushed shoreward under wave inertia. This has also been simulated (Aghsaee *et al.* 2010) and experimentally observed (Michallet & Ivey 1999; Allshouse & Swinney 2020) by others. However, in the present mild-slope experiments (§ 4.1), all boluses were formed by transformation of an NLIW of elevation without intense mixing, as in the experiments by Wallace & Wilkinson (1988). Aghsaee *et al.* (2010) distinguished between ISWs of elevation with trapped cores and the turbulent boluses that emerged from collapsing breakings. However, their 2-D model was unable to resolve 3-D instability in the boluses after fission, which led to an overestimation of wave inertia during breaking and reduced mixing by secondary spanwise instabilities, relative to the 3-D case (Fringer & Street 2003; Aghsaee *et al.* 2010; Arthur & Fringer 2016). Therefore, in general, a bolus formed by fission from an NLIW of depression (mild slope) will have less mixing than boluses generated on steep slopes, as it is initialized from a wave with minimal reflection.

Xu & Stastna (2020) used a 3-D model (SPINS), restricted to two dimensions because of the computational cost, to simulate fission, where an ISW of elevation shoaled after the turning point. A separation bubble gradually developed beneath the wave and eventually broke down into two parts (their figures 3 and 5): one trapped inside the wave; and the other shed behind the leading wave to interact with the trailing waves. Their simulation of separation bubble breakdown provides insight into our bolus formation mechanism. We observed formation of a quasi-trapped core (figure 13*c*; see § 4.3.1) within the bolus and shear instability through the pycnocline, particularly along the rear face. This is where the velocities induced by the wave were maximum and they modelled strong cross-boundary-layer transport. Therefore, where the separation bubble broke down and shear instabilities formed through the wave boundary layer (Ma *et al.* 2016), the NLIW of elevation evolved into a bolus (figure 10).

Comparing the local bolus propagation speed C_b (from the video) with the local fluid velocity u_{max} (from the ADVP) at the bolus birth point for runs 2, 5 and 7 (table 2), we evaluated the Lamb (2002, 2003) criterion, where a trapped core will form when $u_{max} > C_b$. This criterion was valid for all boluses, with our observations showing the wave-induced current became unsteady at the bolus birth point and a quasi-trapped core formed inside of the NLIW of elevation (figure 13*c*; see § 4.3.1) and became a bolus (figure 10). These observations are consistent with the simulations by Xu *et al.* (2016). At the bolus birth point, $u_{max} \approx 0.7c_0$, as observed for a NLIW degenerating through plunging breaking (Boegman & Ivey 2009) following Sveen *et al.* (2002).

The location of the bolus birth point, for all breaking mechanisms except fission, was near the breaking point and close to the 'surging region' (Aghsaee *et al.* 2010; Moore *et al.* 2016; Allshouse & Swinney 2020). The simulations by Aghsaee *et al.* (2010; their figure 18) introduced an equation for the breaking point and proposed that the breaking point for fission was where the first wave of elevation emerged. However, the present observations show bolus formation to begin at a point between the turning point and the interaction point. Here, shear instabilities form through the pycnocline, owing to separation bubble breakdown, as the NLIW of elevation emerges (figure 11). Regressing the bolus birth point against Fr (2.11) gives an equation ($R^2 = 95\,\%$, normalized root-mean-square error (NRMSE) $= 12.9\,\%$) to predict the location of bolus birth for fission on a mild slope (figure 12*a*):

$$\frac{x_{bf}}{L_w} = 3.35Fr^{0.85}. \tag{4.1}$$

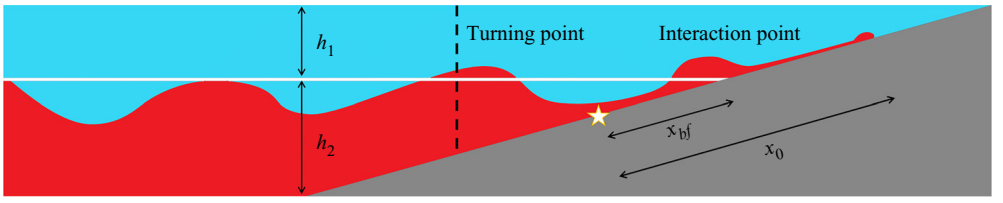

Figure 11. Schematic showing fission of a train of NLIWs of depression over a mild slope. Here, x_{bf} is the distance between the bolus birth point (star) and the interaction point and x_0 is the bolus propagation distance.

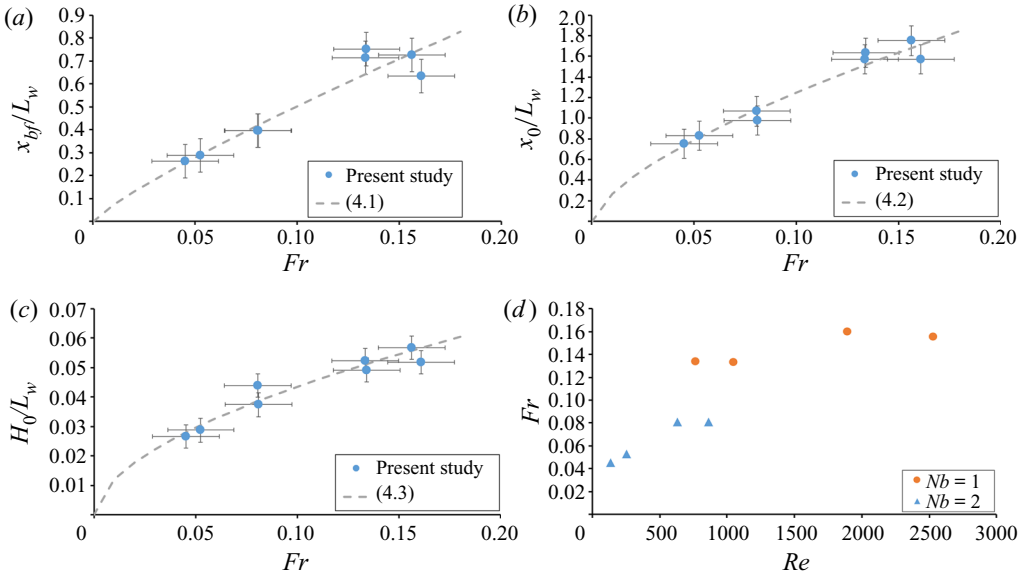

Figure 12. Parameterization of bolus characteristics. (*a*) Bolus birth point criterion: ratio of the distance between the bolus birth point and the interaction point (x_{bf}) normalized by L_w (2.6) versus Fr (2.11). (*b*) The total bolus propagation distance (x_0) normalized by L_w versus Fr. (*c*) The initial height of the bolus (H_0) normalized by L_w versus Fr. (*d*) Classification of number of boluses (Nb) birthed during shoaling of each NLIW of depression in relation to the initial wave forcing parameters Fr and Re (2.10). Data points are mean $\pm$ standard deviation in panels (*a–c*).

Here, x_{bf} is the distance between the bolus birth point and the interaction point and L_w is from (2.6). The bolus birth point was always between the turning and interaction points (figure 11). The location of the bolus birth point, occurring where $u_{max} \approx 0.7c_0$, depended on Fr (ratio of fluid velocity to wave celerity). The bolus birth point moved closer to the turning point as the incident wave energy increased (figure 12*a*) and local current velocities associated with larger incident NLIWs more rapidly approached the local phase speed. Wallace & Wilkinson (1988) also introduced a criterion for the bolus birth point but acknowledged that their results showed large variability and they did not report sufficient data to compare their result with our own.

Moore *et al.* (2016) classified different types of bolus formation according to Fr, Re and the wave steepness ka. They found that $Fr \geq 0.2$ marked a transition from a coherent bolus to a turbulent surge/bore (i.e. a transition from a bolus owing to collapsing to a bolus as a result of either plunging or surging). The Re did not have a considerable effect on the bolus type, except for when $Re < 500$ (or $ka < 0.4$), the bolus would be coherent.

While they did not consider changes in the bottom slope, our results using a mild slope show that the type of bolus depends on the wave-breaking mechanism. The present boluses ($Fr \leq 0.2$ and $ka < 0.4$; table 2) were coherent and $Re > 500$ for all experiments, except runs 1 and 3. Inspection of the observed boluses and their mean velocity profiles (not shown) shows that v increases with Reynolds number, causing more shear instabilities and more mixing with associated energy loss.

4.3. *Bolus characteristics*

The boluses observed in this study were all similar in shape (figure 8), with shear instabilities through the pycnocline, especially along the rear face (e.g. Wallace & Wilkinson 1988; Helfrich 1992; Venayagamoorthy & Fringer 2007; Arthur & Fringer 2014). However, the boluses were not identical, therefore, we investigated what parameters led to changes in the physical characteristics of the boluses.

4.3.1. *Bolus dynamics*

Spatial velocity distributions, under a frozen-time assumption, were computed by multiplying the velocity profile time series (figure 9) by the local bolus propagation speed C_b. The spatial horizontal velocity distribution, for the bolus in figure 9, and the corresponding velocity vector field in the horizontal–vertical plane showed circulation around the bolus, with an upslope flow inside the bolus and downslope flow above (figure 13*a*). The centre of the circulation was considered to be the top of the bolus ($x \approx 41$ cm and depth ≈ 8 cm) and the distance to the bottom was the bolus height H_b. The bolus length L_b was equal to the distance along the bed between where $\bar{U} \approx 0$ m s^{-1} ($x \approx 20$ and 58 cm).

Overlaying the vector field on the corresponding video (figure 13*b*) provided an image similar to field observations by Bourgault *et al.* (2014; their figure 13) both in the St. Lawrence Estuary and in their Reynolds-averaged model. Venayagamoorthy & Fringer (2007) and Vieira & Allshouse (2020) also showed visually similar velocity vectors superimposed on the density contours for one of their simulated boluses (their figures 15*a* and 4*d*, respectively); although the formation mechanisms were different. Jones *et al.* (2020) presented similar velocity vectors superimposed on temperature observations of a bolus on the Australian North West Shelf.

The top of the bolus found from the velocity vectors (centre of the circulation) was inside the bolus – as visualized from the video camera (figure 13*b*) – in agreement with field observations by Bourgault *et al.* (2014; their figure 13). The red fluid above the centre of the circulation is the mixed-density downslope flow (Wallace & Wilkinson 1988; their figure 9) created by shear instabilities through the pycnocline (Venayagamoorthy & Fringer 2007).

The bolus-induced currents may lead to sediment resuspension (Hosegood *et al.* 2004; Boegman & Stastna 2019). At the front face of the bolus, close to the bed (figure 13*b*; $x = 58$ cm), an upward flow may lift bed material, similar to the field-scale model results by Bourgault *et al.* (2014; their figure 13*b*). However, the lack of near-bed velocity data makes interpretation of the resuspension mechanism difficult from backscatter observations both in the field (Richards *et al.* 2013, their figure 9; Klymak & Moum 2003, their figure 5; Jones *et al.* 2020, their figure 3*e*) and in the lab (Aghsaee & Boegman 2015).

Streamlines were generated by subtracting C_b from $\bar{U}$ (Wallace & Wilkinson 1988; Venayagamoorthy & Fringer 2007) to achieve a reference frame moving with the wave (figure 13*c*). The streamlines show a quasi-trapped core (e.g. Lamb 2002, 2003; Klymak

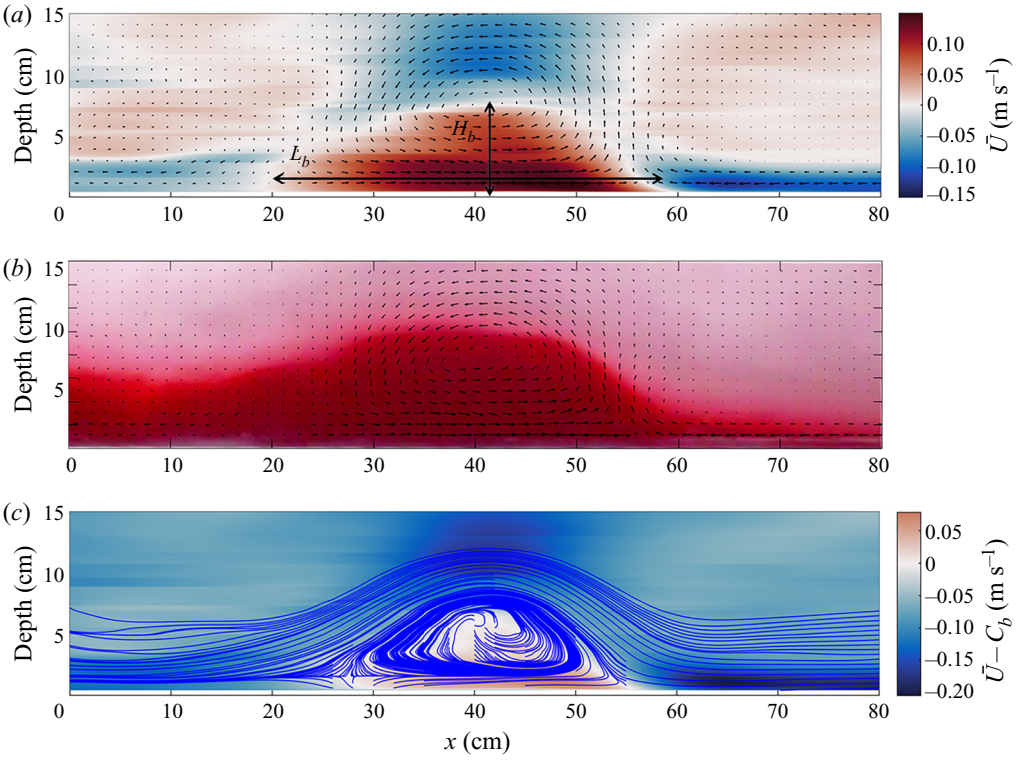

Figure 13. Flow within a bolus. (*a*) Spatial distribution of the $\bar{U}$ velocity superimposed on the 2-D velocity vector field for a bolus from run 8 as captured by the first ADVP. (*b*) The 2-D velocity vector field superimposed on a video image of the bolus in panel (*a*). (*c*) Streamlines from a reference frame moving with the wave for the bolus in panel (*a*). In all panels, the bolus moves from left to right.

& Moum 2003), which is thought to carry sediments along the continental shelf (Richards *et al.* 2013; Bourgault *et al.* 2014). The size of the bolus decreased while moving upslope, owing to drainage of the core by the return flow and mixing between the core and the ambient fluid (Xu *et al.* (2016), which confirmed the appropriateness of using 'quasi-trapped core' terminology to describe the boluses. The largest closed streamline passed over the top of the bolus, which showed that the boundary of the quasi-trapped core region was the same as what we considered to be the bolus. Venayagamoorthy & Fringer (2007) identified two circulation regions within the bolus: one was larger and in the upper portion of the bolus, which is analogous to figure 13(*c*), and the other was close to the bottom with flow in the reverse direction that caused lower layer fluid to drain from the bolus through the rear face. In figure 13(*c*), there is flow separation beneath the circulating core, but owing to the lack of data close to the bottom, it is not clear if this is the secondary circulation cell modelled by Venayagamoorthy & Fringer (2007). This requires further investigation using neutrally buoyant particles to visualize the near-bed flow. In their comprehensive field observations, Jones *et al.* (2020) did not mention boluses with trapped cores, rather their most observed phenomenon was a solitary-like wave with a trapped core that had a recirculation region centred inside the wave (their figure 3*a*). We did not observe these waves in the present observations (e.g. figure 10).

To relate bolus propagation speed to the initial wave forcing, Moore *et al.* (2016) plotted the $C_b/\omega a$ versus Fr (figure 14*a*) and ka (figure 14*b*). Despite the bolus generation

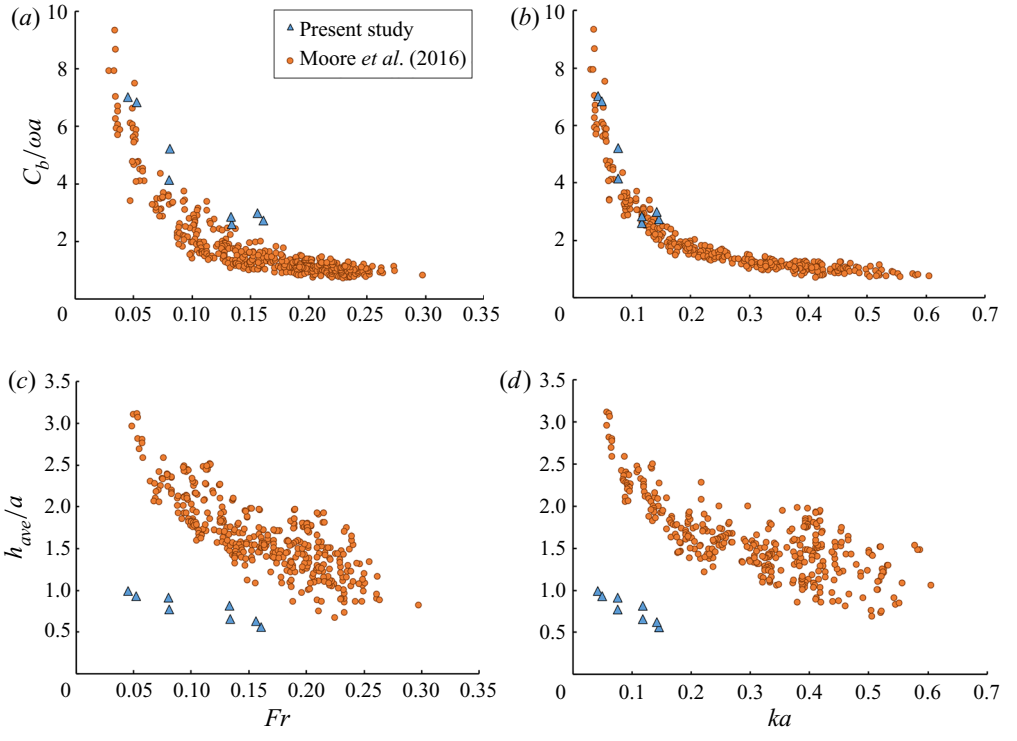

Figure 14. Local bolus propagation speed (C_b) (normalized by ωa) versus (a) wave Froude number (Fr) and (b) wave steepness (ka). Average bolus height (h_{ave}) (normalized by a) versus (c) wave Froude number (Fr), (d) wave steepness (ka).

mechanisms being different, our data agree with their trend, showing that by increasing the initial wave forcing, the normalized bolus speed decreased. Moore *et al.* (2016) proposed that this was because some of the incident wave energy was lost to turbulence and when the bolus became unstable, more energy would be dissipated. Although they did not generate boluses by fission, our observations also show that for the runs with higher wave forcing ($Re > 500$), the edges of the boluses were more irregular with instability-driven mixing.

4.3.2. *Bolus propagation distance*

It is important to know the total distance a bolus will propagate after formation, transporting cold dense fluid, sediments and nutrients. Figure 12(b) shows the bolus propagation distance x_0 normalized by L_w (2.6), relative to Fr (2.11). Regression data gives an equation for bolus propagation distance ($R^2 = 96\,\%$, NRMSE $= 8.2\,\%$):

$$\frac{x_0}{L_w} = 5.81 Fr^{0.67}. \tag{4.2}$$

Larger incident waves, with more fluid inertia and greater Fr, will form boluses that propagate further upslope (figure 12b).

4.3.3. *Bolus size*

The size of a bolus has been shown to consistently diminish as it propagates upslope in both process-based investigations (figures 5–8; Wallace & Wilkinson 1988;

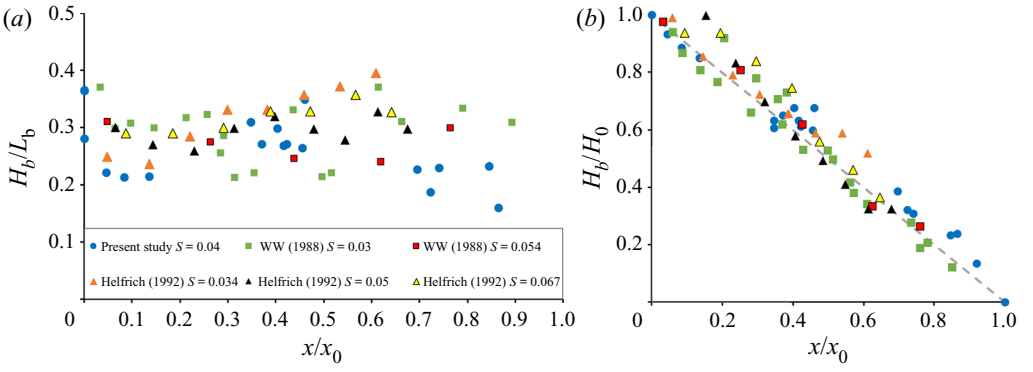

Figure 15. Parameterizations for bolus aspect ratio. (*a*) The bolus height-to-length ratio as a function of the normalized distance from the bolus birth point. The ordinate scale is the distance of the bolus from the bolus birth point (x) normalized by the bolus propagation distance (x_0). (*b*) Variation of normalized bolus height (H_0 = initial bolus height) versus the distance to the bolus from the bolus birth point (x) normalized by the bolus propagation distance (x_0). Wallace & Wilkinson (1988) is referred to as WW (1988).

Helfrich 1992; Moore *et al.* 2016; Allshouse & Swinney 2020) and field observations (Sandstrom & Elliott 1984; Moum *et al.* 2007; Bourgault *et al.* 2014). The bolus height-to-length ratio $H_b/L_b \approx 0.3$ (figure 15*a*) remained approximately constant (Wallace & Wilkinson 1988). Figure 15(*b*) shows that the change in H_b from the initial bolus height (H_o) through bolus degeneration is linear (Wallace & Wilkinson 1988; Helfrich 1992, their (8); Bourgault *et al.* 2007). This is independent of whether the boluses were generated from NLIWs of elevation (Wallace & Wilkinson 1988), collapsing NLIWs of depression (Helfrich 1992) or fission (present study).

To parameterize H_o, Helfrich (1992) proposed $H_0/a = 1.75 \pm 0.25$ for $0 < \lambda_{KdV}/L_i < 0.25$, which was shown by Aghsaee *et al.* (2010) to decrease with increasing λ_{KdV}/L_i (figure S5). However, all of our NLIWs ($0.24 \leq a/h_1 \leq 0.55$), most of the NLIWs in Aghsaee *et al.* (2010) ($0.2 \leq a/h_1 \leq 2.05$) and some of the NLIWs in Helfrich (1992) ($0.07 \leq a/h_1 \leq 3.4$) were not of the weakly nonlinear KdV-type (i.e. $a/h_1 > 0.22$, Cui *et al.* 2021). Consequently, $\lambda > \lambda_{KdV}$, bringing into question the utility of this parameterization. To better classify surging and collapsing breakers, Aghsaee *et al.* (2010) introduced the parameter H_0/H_t, where H_t is the depth where the separation bubble has reached the pycnocline. However, we found that this criterion was not applicable to breaking by fission, as the separation bubble split before reaching the pycnocline. Therefore, there was a need for a new relation to predict H_o for fission.

Motivated by the results of Moore *et al.* (2016) and given the data scatter (figure S5), we predicted the initial height of the bolus (normalized by L_w) relative to Fr ($R^2 = 94\,\%$, NRMSE = 9.5 %):

$$\frac{H_0}{L_w} = 0.16 Fr^{0.56}. \tag{4.3}$$

The waves became taller and narrower as Fr increased (figure 12*c*). This observation was surprising, given that field data shows higher frequency NLIWs to have taller (sech^2 versus sinusoidal) profiles and less energy (Boegman et al 2005; their figure 15). We surmise that Fr is locally regulated by shoaling, enhancing u_{max} relative to C_b.

The relation of the average bolus height ($h_{ave} = H_0/2$) normalized by the incident wave amplitude to wave inertia and steepness (figures 14*c* and 14*d*) were also investigated, as in Moore *et al.* (2016). The average bolus height decreased with increasing wave inertia, as

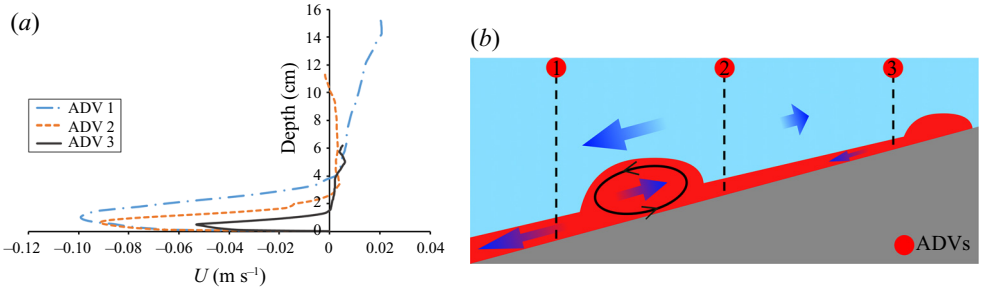

Figure 16. (*a*) Mean velocity profiles of the return flow at the ADVP for run 8. (*b*) Schematic showing boluses propagating over the boundary slope, with fluid draining to a return flow. In panel (*a*), the mean velocities for depth <0.5 cm are modelled by using the log-law.

energy was lost to turbulence and drag. The discrepancy between our results and those of Moore *et al.* (2016) results from the differences in incident wave types (periodic sinusoidal internal waves versus NLIWs of depression) and, as a result, different definitions of wave amplitude. We have also chosen a different criterion for bolus height (§ 4.2.1), using the top of the bolus to be the inflection point in the velocity field ($\bar{U} = 0$; figure 13*a*), whereas Moore *et al.* (2016) chose the pycnocline (e.g. figure 13*b*). We believe that our definition is more conceptually sound, as it is based on the finding boundary between the upslope moving bolus and downslope return flow. Moreover, this will be easier to locate in profiles from moorings, considering that the height of the bolus is a function of pycnocline thickness (Vieira & Allshouse 2020).

Given the decrease in bolus size as it shoals, it remains important to quantify how much of the lower layer fluid contained in the bolus is lost to irreversible mixing with the upper layer, relative to what is lost to the near-bed return flow (Southard & Cacchione 1972). We do not have sufficient data for a complete analysis; however, we were able to estimate the return flow from the mean velocity profiles for run 8 (figure 16*a*). The return flow thickness and velocity were observed to decrease as the boluses shoaled. Taking a control volume between ADV-1 and ADV-3 (figure 16*b*), the change in bolus volume was estimated from the digitized video images (not shown) as $\Delta V1 \approx V_{\text{ADV-1}} - V_{\text{ADV-3}} \approx 0.025 - 0.003 \approx 0.022 \pm 0.01$ m^3. This was compared with the volume flux in the return flow at these two points (figure 16*a*) and the travel time of the bolus from ADV-1 to ADV-3 as $\Delta V2 \approx \Delta t \times \Delta Q \approx 19.8 \times 0.0012 \approx 0.023 \pm 0.01$ m^3. The computed values for $\Delta V1$ and $\Delta V2$ were within the error bounds associated with estimating the density profiles of the return flow and the bolus. This back-of-the-envelope example suggests that, for this case, the bulk of the bolus core may be lost to the return flow, with irreversible mixing of bolus fluid to the upper fluid layer (e.g. as required for nutrient flux) being minimal. Here, we have neglected transport and mixing that may occur owing to other mechanisms and at different stages of bolus evolution. For example, Xu & Stastna (2020) showed that when boluses started to form, significant cross-boundary-layer transport could occur. Given the implications for nutrient supply to the continental shelf, these back-of-the-envelope calculations should be investigated further.

4.3.4. *Number of boluses*

From the literature, it remains unclear how many boluses to expect from each incident NLIW of depression. For a lone NLIW of depression, a different number of boluses will be generated depending on the characteristics of the wave and the slope (Aghsaee *et al.* 2010;

their figure 13). For a packet of two incident ISWs of depression, Helfrich (1992) observed that the first wave formed only one bolus, but for the second wave, the number of boluses was the same as the number of boluses for a similar lone wave (see their figure 18). For ISWs of elevation, Wallace & Wilkinson (1988) found one bolus for each wave, as did Moore *et al.* (2016) for each wave in a train of sinusoidal internal waves.

We observed either one or two boluses to be generated from a single NLIW of depression; matching the number of NLIWs of elevation formed during fission after the turning point (Wallace & Wilkinson (1988). The number of NLIWs of elevation generated by fission depended on the characteristics of the incident NLIW of depression. Malomed & Shrira (1991) proposed a KdV-based equation to predict the number of secondary solitons (ISWs of elevation), but as with Helfrich (1992) and Aghsaee *et al.* (2010), this relationship only worked when there was a lone ISW of depression; not a periodic train, as in the present study.

The number of boluses increased as both Froude number (2.11) and Reynolds number (2.10) decreased; with $Fr \approx 0.1$ separating the data (figure 12*d*). The decreasing number of boluses, with increasing wave inertia (Fr), can be interpreted according to the generation time scale for each NLIW of elevation. Each NLIW of depression has a finite 'duration of transition' (Grimshaw *et al.* 1998; transformation time scale from an NLIW of depression to a packet of NLIWs of elevation). Increasing Fr causes the wave period to decrease and each NLIW of depression has a shorter duration of transition, before the arrival of the next NLIW in the packet, which prevents further boluses from forming (§ 3.2; figure 7).

5. Conclusions

The present study extends the prior work on NLIW fission and bolus formation on mild slopes as commonly observed in lakes and continental margins. As each NLIW of depression shoals, they evolve into a packet of NLIWs of elevation after passing the turning point; the number of waves of elevation depends on the Froude number of the incident wave. The waves of elevation transform into boluses where shear instability occurs through the pycnocline. At this 'bolus birth point', flow velocities are maximum. Each bolus propagates upslope as a quasi-trapped core, decreasing in size and velocity magnitude, through loss of volume to a near-bed return flow emanating from the rear face and diapycnal mixing from instability across the pycnocline. A simple calculation suggests that for some cases, the volume-flux to the return flow may predominate, thereby limiting the overall effectiveness of some boluses in driving biogeochemical fluxes in the coastal ocean. However, this topic requires further research as both shear and lobe-cleft instabilities were observed to drive mixing, which was not quantified experimentally.

The formation mechanism, birth point, propagation distance and initial height of the boluses generated from fission were distinct from those generated by other breaking mechanisms associated with NLIWs of depression or elevation, but the height to length ratio, change in size with propagation and the velocity field inside and around the boluses were all remarkably similar. The bolus birth point, initial height and dissipation length scale were parameterized in terms of variables that are measurable in the field by oceanographers. These bolus characteristics were related to Fr, with $u_{max} \approx 0.7c_0$ at the bolus birth point. Future work should investigate effects of changing the boundary slope ($S \leq 0.05$) as well as the generality of the equations describing the bolus birth point, the initial bolus height and the total bolus propagation distance. We are presently extending this study to investigate sediment resuspension and transport by fission and bolus propagation over mild slopes.

Supplemental material and movies. Supplementary material and movies are available at https://doi.org/10.1017/jfm.2021.1033.

Acknowledgements. We thank R. Mulligan for lending us two Vectrino ADVPs for use in the lab. L.B. thanks J. Moum for pointing out that we experimentalists were using slopes that were different from what is actually in the coastal ocean. L.B. thanks N. Jones and G. Ivey for discussions on the challenges in measuring NLIW transformation between moorings. We thank P. Davies and J. Grue for an invitation to present our early findings from this study at the 6th Norway–Scotland Waves & Marine Hydrodynamics Symposium. Four anonymous reviewers are thanked for their constructive and valuable comments. Upon acceptance for publication, the laboratory data will be archived in the Dataverse repository at Queen's University (https://dataverse.scholarsportal.info/).

Funding. This research was funded by an NSERC Discovery Grant and Discovery Accelerator Supplement to L.B. and by Queen's University.

Declaration of interests. The authors report no conflict of interest.

Author ORCIDs.
Amin Ghassemi https://orcid.org/0000-0003-2587-2916;
Leon Boegman https://orcid.org/0000-0001-9492-9248.

References

Aghsaee, P. & Boegman, L. 2015 Experimental investigation of sediment resuspension beneath internal solitary waves of depression. *Journal of Geophysical Research: Oceans* **120**, 3301–3314.

Aghsaee, P., Boegman, L. & Lamb, K.G. 2010 Breaking of shoaling internal solitary waves. *Journal of Fluid Mechanics* **659**, 289–317.

Ahmari, H. 2013 Size, dynamics and consequences of large-scale horizontal coherent structures in open-channel flows: an experimental study. PhD thesis, Queen's University.

Allshouse, M.R. & Swinney, H.L. 2020 Dependence of internal wave bolus transport on pycnocline thickness. *Geophysical Research Letters* **47**, e2020GL086952.

Apel, J.R. 2002 Oceanic internal waves and solitons. An atlas of oceanic internal solitary waves. Global Ocean Associates. Prepared for the Office of Naval Research, USA, Code 322PO, pp. 1–40.

Apel, J.R., Holbrook, J.R., Liu, A.K. & Tsai, J.J. 1985 The Sulu Sea internal soliton experiment. *Journal of Physical Oceanography* **15**, 1625–1651.

Arthur, R.S. & Fringer, O.B. 2014 The dynamics of breaking internal solitary waves on slopes. *Journal of Fluid Mechanics* **761**, 360–398.

Arthur, R.S. & Fringer, O.B. 2016 Transport by breaking internal gravity waves on slopes. *Journal of Fluid Mechanics* **789**, 93–126.

Barad, M.F. & Fringer, O.B. 2010 Simulations of shear instabilities in interfacial gravity waves. *Journal of Fluid Mechanics* **644**, 61–95.

Boegman, L., Imberger, J., Ivey, G.N. & Antenucci, J.P. 2003 High-frequency internal waves in large stratified lakes. *Limnology and oceanography* **48**, 895–919.

Boegman, L. & Ivey, G.N. 2009 Flow separation and resuspension beneath shoaling nonlinear internal waves. *Journal of Geophysical Research: Oceans* **114**, C02018.

Boegman, L. & Ivey, G.N. 2012 The dynamics of internal wave resonance in periodically forced narrow basins. *Journal of Geophysical Research: Oceans* **117**, C11002.

Boegman, L., Ivey, G. & Imberger, J. 2005 The degeneration of internal waves in lakes with sloping topography. *Limnology and Oceanography* **50**, 1620–1637.

Boegman, L. & Stastna, M. 2019 Sediment resuspension and transport by internal solitary waves. *Annual Review of Fluid Mechanics* **51**, 129–154.

Bogucki, D., Dickey, T. & Redekopp, L.G. 1997 Sediment resuspension and mixing by resonantly generated internal solitary waves. *Journal of Physical Oceanography* **27**, 1181–1196.

Bouffard, D., Boegman, L. & Rao, Y.R. 2012 Poincaré wave–induced mixing in a large lake. *Limnology and Oceanography* **57**, 1201–1216.

Bourgault, D., Blokhina, M., Mirshak, R. & Kelley, D. 2007 Evolution of a shoaling internal solitary wavetrain. *Geophysical Research Letters* **34**, L03601.

Bourgault, D., Kelley, D.E. & Galbraith, P.S. 2005 Interfacial solitary wave run-up in the St. Lawrence Estuary. *Journal of Marine Research* **63**, 1001–1015.

BOURGAULT, D., MORSILLI, M., RICHARDS, C., NEUMEIER, U. & KELLEY, D.E. 2014 Sediment resuspension and nepheloid layers induced by long internal solitary waves shoaling orthogonally on uniform slopes. *Continental Shelf Research* **72**, 21–33.

CACCHIONE, D., PRATSON, L.F. & OGSTON, A. 2002 The shaping of continental slopes by internal tides. *Science* **296**, 724–727.

CARR, M. & DAVIES, P. 2010 Boundary layer flow beneath an internal solitary wave of elevation. *Physics of Fluids* **22**, 026601.

CARTER, G.S., GREGG, M.C. & LIEN, R.-C. 2005 Internal waves, solitary-like waves, and mixing on the Monterey Bay shelf. *Continental Shelf Research* **25**, 1499–1520.

CHANSON, H. 2008 Acoustic doppler velocimetry (ADV) in the field and in laboratory: practical experiences. In *Proceedings of the International Meeting on Measurementsand Hydraulics of Sewers IMMHS'08, Summer School GEMCEA/LCPC*, 19–21 August 2008, Bouguenais (ed. F. Larrarte & H. Chanson), Hydraulic Model Report No. CH70/08, pp. 49–66. Division of Civil Engineering, The University of Queensland, Brisbane, Australia.

CUI, J., DONG, S. & WANG, Z. 2021 Study on applicability of internal solitary wave theories by theoretical and numerical method. *Applied Ocean Research* **111**, 102629.

FRINGER, O.B. & STREET, R.L. 2003 The dynamics of breaking progressive interfacial waves. *Journal of Fluid Mechanics* **494**, 319–353.

FRUCTUS, D., CARR, M., GRUE, J., JENSEN, A. & DAVIES, P.A. 2009 Shear induced breaking of large internal solitary waves. *Journal of Fluid Mechanics* **620**, 1–29.

GÍMEZ-GIRALDO, A., IMBERGER, J., ANTENUCCI, J.P. & YEATES, P.S. 2008 Wind-shear-generated high-frequency internal waves as precursors to mixing in a stratified lake. *Limnology and Oceanography* **53**, 354–367.

GOREAU, T., MCCLANAHAN, T., HAYES, R. & STRONG, A. 2000 Conservation of coral reefs after the 1998 global bleaching event. *Conservation Biology* **14**, 5–15.

GRIMSHAW, R., PELINOVSKY, E. & TALIPOVA, T. 1998 Solitary wave transformation due to a change in polarity. *Studies in Applied Mathematics* **101**, 357–388.

GUO, D., ZHAN, P. & HOTEIT, I. 2021 Three-Dimensional Simulation of Shoaling Internal Solitary Waves and Their Influence on Particle Transport in the Southern Red Sea. *Journal of Geophysical Research: Oceans* **126**, e2020JC016335.

HALPERN, D. 1969 Observations of short period internal waves in Massachusetts Bay. PhD Thesis, Massachusetts Institute of Technology.

HÄRTEL, C., CARLSSON, F. & THUNBLOM, M. 2000 Analysis and direct numerical simulation of the flow at a gravity-current head. Part 2. The lobe-and-cleft instability. *Journal of Fluid Mechanics* **418**, 213–229.

HAURY, L.R., BRISCOE, M.G. & ORR, M.H. 1979 Tidally generated internal wave packets in Massachusetts Bay. *Nature* **278**, 312–317.

HAWLEY, N. 2004 Response of the benthic nepheloid layer to near-inertial internal waves in southern Lake Michigan. *Journal of Geophysical Research: Oceans* **109**, C04007.

HELFRICH, K.R. 1992 Internal solitary wave breaking and run-up on a uniform slope. *Journal of Fluid Mechanics* **243**, 133–154.

HELFRICH, K.R. & MELVILLE, W. 1986 On long nonlinear internal waves over slope-shelf topography. *Journal of Fluid Mechanics* **167**, 285–308.

HELFRICH, K.R. & MELVILLE, W.K. 2006 Long nonlinear internal waves. *Annu. Rev. Fluid Mech* **38**, 395–425.

HOLLOWAY, P.E. 1987 Internal hydraulic jumps and solitons at a shelf break region on the Australian North West Shelf. *Journal of Geophysical Research: Oceans* **92**, 5405–5416.

HOLLOWAY, P.E., CHATWIN, P.G. & CRAIG, P. 2001 Internal tide observations from the Australian North West Shelf in summer 1995. *Journal of Physical Oceanography* **31**, 1182–1199.

HORN, D., IMBERGER, J. & IVEY, G. 2001 The degeneration of large-scale interfacial gravity waves in lakes. *Journal of Fluid Mechanics* **434**, 181–207.

HOSEGOOD, P., BONNIN, J. & VAN HAREN, H. 2004 Solibore-induced sediment resuspension in the Faeroe-Shetland Channel. *Geophysical Research Letters* **31**, L09301.

HULT, E.L., TROY, C.D. & KOSEFF, J.R. 2010 Harmonic generation of interfacial waves at a submerged bathymetric ridge. *Journal of Geophysical Research: Oceans* **115**, C02001.

IVEY, G. & NOKES, R. 1989 Vertical mixing due to the breaking of critical internal waves on sloping boundaries. *Journal of Fluid Mechanics* **204**, 479–500.

JACKSON, C. 2007 Internal wave detection using the moderate resolution imaging spectroradiometer (MODIS). *Journal of Geophysical Research: Oceans* **112**, C11012.

JACKSON, C.R., DA SILVA, J.C. & JEANS, G. 2012 The generation of nonlinear internal waves. *Oceanography* **25**, 108–123.

JONES, N., IVEY, G., RAYSON, M. & KELLY, S. 2020 Mixing driven by breaking nonlinear internal waves. *Geophysical Research Letters* **47**, e2020GL089591.

KARL, H., CACCHIONE, D. & CARLSON, P. 1986 Internal-wave currents as a mechanism to account for large sand waves in Navarinsky Canyon head, Bering Sea. *Journal of Sedimentary Research* **56**, 706–714.

KLYMAK, J.M. & MOUM, J.N. 2003 Internal solitary waves of elevation advancing on a shoaling shelf. *Geophysical Research Letters* **30** (20), 2045.

LAMB, K.G. 1994 Numerical experiments of internal wave generation by strong tidal flow across a finite amplitude bank edge. *Journal of Geophysical Research: Oceans* **99**, 843–864.

LAMB, K.G. 2002 A numerical investigation of solitary internal waves with trapped cores formed via shoaling. *Journal of Fluid Mechanics* **451**, 109–144.

LAMB, K.G. 2003 Shoaling solitary internal waves: on a criterion for the formation of waves with trapped cores. *Journal of Fluid Mechanics* **478**, 81–100.

LAMB, K.G. 2014 Internal wave breaking and dissipation mechanisms on the continental slope/shelf. *Annual Review of Fluid Mechanics* **46**, 231–254.

LAMB, K. & WARN-VARNAS, A. 2015 Two-dimensional numerical simulations of shoaling internal solitary waves at the ASIAEX site in the South China Sea. *Nonlinear Processes in Geophysics* **22**, 289–312.

LAMB, K.G. & XIAO, W. 2014 Internal solitary waves shoaling onto a shelf: Comparisons of weakly-nonlinear and fully nonlinear models for hyperbolic-tangent stratifications. *Ocean Modelling* **78**, 17–34.

LEICHTER, J.J., WING, S.R., MILLER, S.L. & DENNY, M.W. 1996 Pulsed delivery of subthermocline water to Conch Reef (Florida Keys) by internal tidal bores. *Limnology and Oceanography* **41**, 1490–1501.

LIM, K., IVEY, G. & JONES, N. 2010 Experiments on the generation of internal waves over continental shelf topography. *Journal of Fluid Mechanics* **663**, 385–400.

MA, X., YAN, J., HOU, Y., LIN, F. & ZHENG, X. 2016 Footprints of obliquely incident internal solitary waves and internal tides near the shelf break in the northern South China Sea. *Journal of Geophysical Research: Oceans* **121**, 8706–8719.

MACINTYRE, S., FLYNN, K.M., JELLISON, R. & ROMERO, J.R. 1999 Boundary mixing and nutrient fluxes in Mono Lake, California. *Limnology and Oceanography* **44**, 512–529.

MALOMED, B.A. & SHRIRA, V.I. 1991 Soliton caustics. *Physica D: Nonlinear Phenomena* **53**, 1–12.

MASUNAGA, E., ARTHUR, R.S., FRINGER, O.B. & YAMAZAKI, H. 2017 Sediment resuspension and the generation of intermediate nepheloid layers by shoaling internal bores. *Journal of Marine Systems* **170**, 31–41.

MCLELLAND, S.J. & NICHOLAS, A.P. 2000 A new method for evaluating errors in high-frequency ADV measurements. *Hydrological Processes* **14**, 351–366.

MCPHEE-SHAW, E. 2006 Boundary–interior exchange: reviewing the idea that internal-wave mixing enhances lateral dispersal near continental margins. *Deep Sea Research Part II: Topical Studies in Oceanography* **53**, 42–59.

MICHALLET, H. & IVEY, G. 1999 Experiments on mixing due to internal solitary waves breaking on uniform slopes. *Journal of Geophysical Research: Oceans* **104**, 13467–13477.

MOORE, C.D., KOSEFF, J.R. & HULT, E.L. 2016 Characteristics of bolus formation and propagation from breaking internal waves on shelf slopes. *Journal of Fluid Mechanics* **791**, 260–283.

MOUM, J., FARMER, D., SMYTH, W., ARMI, L. & VAGLE, S. 2003 Structure and generation of turbulence at interfaces strained by internal solitary waves propagating shoreward over the continental shelf. *Journal of Physical Oceanography* **33**, 2093–2112.

MOUM, J., KLYMAK, J., NASH, J., PERLIN, A. & SMYTH, W. 2007 Energy transport by nonlinear internal waves. *Journal of Physical Oceanography* **37**, 1968–1988.

NAKAYAMA, K. & IMBERGER, J. 2010 Residual circulation due to internal waves shoaling on a slope. *Limnology and Oceanography* **55**, 1009–1023.

NAKAYAMA, K., SATO, T., SHIMIZU, K. & BOEGMAN, L. 2019 Classification of internal solitary wave breaking over a slope. *Physical Review Fluids* **4**, 014801.

NAKAYAMA, K., SHINTANI, T., KOKUBO, K., KAKINUMA, T., MARUYA, Y., KOMAI, K. & OKADA, T. 2012 Residual currents over a uniform slope due to breaking of internal waves in a two-layer system. *Journal of Geophysical Research: Oceans* **117**, C10002.

NIKORA, V. & GORING, D. 2000 Eddy convection velocity and Taylor's hypothesis of 'frozen' turbulence in a rough-bed open-channel flow. *Journal of hydroscience and hydraulic engineering* **18**, 75–91.

ORR, M.H. & MIGNEREY, P.C. 2003 Nonlinear internal waves in the South China Sea: Observation of the conversion of depression internal waves to elevation internal waves. *Journal of Geophysical Research: Oceans* **108** (C3), 3064.

OSBORNE, A. & BURCH, T. 1980 Internal solitons in the Andaman Sea. *Science* **208**, 451–460.
OSTROVSKY, L. & STEPANYANTS, Y.A. 2005 Internal solitons in laboratory experiments: Comparison with theoretical models. *Chaos: An Interdisciplinary Journal of Nonlinear Science* **15**, 037111.
POMAR, L., MORSILLI, M., HALLOCK, P. & BÁDENAS, B. 2012 Internal waves, an under-explored source of turbulence events in the sedimentary record. *Earth-Science Reviews* **111**, 56–81.
PUIG, P., PALANQUES, A., GUILLÉN, J. & EL KHATAB, M. 2004 Role of internal waves in the generation of nepheloid layers on the northwestern Alboran slope: implications for continental margin shaping. *Journal of Geophysical Research: Oceans* **109**, C09011.
REEDER, D.B., MA, B.B. & YANG, Y.J. 2011 Very large subaqueous sand dunes on the upper continental slope in the South China Sea generated by episodic, shoaling deep-water internal solitary waves. *Marine Geology* **279**, 12–18.
RICHARDS, C., BOURGAULT, D., GALBRAITH, P.S., HAY, A. & KELLEY, D.E. 2013 Measurements of shoaling internal waves and turbulence in an estuary. *Journal of Geophysical Research: Oceans* **118**, 273–286.
RIVERA-ROSARIO, G., DIAMESSIS, P.J., LIEN, R.-C., LAMB, K.G. & THOMSEN, G.N. 2020 Formation of Recirculating Cores in Convectively Breaking Internal Solitary Waves of Depression Shoaling over Gentle Slopes in the South China Sea. *Journal of Physical Oceanography* **50**, 1137–1157.
SANDSTROM, H. & ELLIOTT, J. 1984 Internal tide and solitons on the Scotian Shelf: A nutrient pump at work. *Journal of Geophysical Research: Oceans* **89**, 6415–6426.
SCOTTI, A. & PINEDA, J. 2004 Observation of very large and steep internal waves of elevation near the Massachusetts coast. *Geophysical research letters* **31**, L22307.
SCOTTI, A. & PINEDA, J. 2007 Plankton accumulation and transport in propagating nonlinear internal fronts. *Journal of Marine Research* **65**, 117–145.
SHROYER, E., MOUM, J. & NASH, J. 2009 Observations of polarity reversal in shoaling nonlinear internal waves. *Journal of Physical Oceanography* **39**, 691–701.
SIMPSON, J.E. 1972 Effects of the lower boundary on the head of a gravity current. *Journal of Fluid Mechanics* **53**, 759–768.
SMYTH, W., MOUM, J. & NASH, J. 2011 Narrowband oscillations in the upper equatorial ocean. Part II: Properties of shear instabilities. *Journal of Physical Oceanography* **41**, 412–428.
SOUTHARD, J.B. & CACCHIONE, D. 1972. Experiments on bottom sediment movement by breaking internal waves. In *Shelf Sediment Transport: Process and Pattern* (ed. D.J. Swift, D.B. Duane & O.H. Pilkey), pp. 83–97. Dowden, Hutchinson & Ross.
STANTON, T. & OSTROVSKY, L. 1998 Observations of highly nonlinear internal solitons over the continental shelf. *Geophysical Research Letters* **25**, 2695–2698.
STASTNA, M. & LAMB, K.G. 2008 Sediment resuspension mechanisms associated with internal waves in coastal waters. *Journal of Geophysical Research: Oceans* **113**, C10016.
SUTHERLAND, B., BARRETT, K. & IVEY, G. 2013 Shoaling internal solitary waves. *Journal of Geophysical Research: Oceans* **118**, 4111–4124.
SVEEN, J.K., GUO, Y., DAVIES, P.A. & GRUE, J. 2002 On the breaking of internal solitary waves at a ridge. *Journal of Fluid Mechanics* **469**, 161–188.
THORPE, S. 1978 On the shape and breaking of finite amplitude internal gravity waves in a shear flow. *Journal of Fluid Mechanics* **85**, 7–31.
TROY, C.D. & KOSEFF, J.R. 2005 The instability and breaking of long internal waves. *Journal of Fluid Mechanics* **543**, 107–136.
VENAYAGAMOORTHY, S.K. & FRINGER, O.B. 2007 On the formation and propagation of nonlinear internal boluses across a shelf break. *Journal of Fluid Mechanics* **577**, 137–159.
VIEIRA, G.S. & ALLSHOUSE, M.R. 2020 Internal wave boluses as coherent structures in a continuously stratified fluid. *Journal of Fluid Mechanics* **885**, A35.
VLASENKO, V. & STASHCHUK, N. 2007 Three-dimensional shoaling of large-amplitude internal waves. *Journal of Geophysical Research: Oceans* **112**, C11018.
WALLACE, B. & WILKINSON, D. 1988 Run-up of internal waves on a gentle slope in a two-layered system. *Journal of Fluid Mechanics* **191**, 419–442.
WALTER, R.K., SQUIBB, M.E., WOODSON, C.B., KOSEFF, J.R. & MONISMITH, S.G. 2014 Stratified turbulence in the nearshore coastal ocean: Dynamics and evolution in the presence of internal bores. *Journal of Geophysical Research: Oceans* **119**, 8709–8730.
WALTER, R.K., WOODSON, C.B., ARTHUR, R.S., FRINGER, O.B. & MONISMITH, S.G. 2012 Nearshore internal bores and turbulent mixing in southern Monterey Bay. *Journal of Geophysical Research: Oceans* **117**, C07017.
WEST, J.M. & SALM, R.V. 2003 Resistance and resilience to coral bleaching: implications for coral reef conservation and management. *Conservation Biology* **17**, 956–967.

WÜEST, A., PIEPKE, G. & VAN SENDEN, D.C. 2000 Turbulent kinetic energy balance as a tool for estimating vertical diffusivity in wind-forced stratified waters. *Limnology and Oceanography* **45**, 1388–1400.

WUNSCH, C. 1971 Note on some Reynolds stress effects of internal waves on slopes. In *Deep Sea Research and Oceanographic Abstracts*, pp. 583–591. Elsevier.

XU, C. & STASTNA, M. 2020 Instability and cross-boundary-layer transport by shoaling internal waves over realistic slopes. *Journal of Fluid Mechanics* **895**, R6.

XU, C., SUBICH, C. & STASTNA, M. 2016 Numerical simulations of shoaling internal solitary waves of elevation. *Physics of Fluids* **28**, 076601.

ZULBERTI, A., JONES, N. & IVEY, G. 2020 Observations of enhanced sediment transport by nonlinear internal waves. *Geophysical Research Letters* **47**, e2020GL088499.